

Minimum tracking linear response Hubbard and Hund corrected Density Functional Theory in CP2K

Ziwei Chai^{1,#}, Rutong Si², Mingyang Chen³, Gilberto Teobaldi⁴, David D. O'Regan⁵, Li-Min Liu^{2*}

- 1 Beijing Computational Science Research Center, Beijing, 100193, China
- 2 School of Physics, Beihang University, Beijing 100191, China
- 3 School of Materials Science and Engineering, University of Science and Technology Beijing, Beijing, 100083, China
- 4 Scientific Computing Department, STFC UKRI, Rutherford Appleton Laboratory, Harwell Campus, OX11 0QX Didcot, United Kingdom
- 5 School of Physics, SFI AMBER Centre and CRANN Institute, Trinity College Dublin, The University of Dublin, Ireland

Email: liminliu@buaa.edu.cn

Present address: Department of Chemistry, University of Zurich, Winterthurerstrasse 190, 8057 Zurich, Switzerland

ABSTRACT

We present the implementation of the Hubbard (U) and Hund (J) corrected Density Functional Theory (DFT+U+J) functionality in the Quickstep program, which is part of the CP2K suite. The tensorial and Löwdin subspace representations are implemented and compared. Full analytical DFT+U+J forces are implemented and benchmarked for the tensorial and Löwdin representations. We also present the implementation of the recently proposed minimum-tracking linear-response method that enables the U and J parameters to be calculated on first principles basis without reference to the Kohn-Sham eigensystem. These implementations are benchmarked against recent results for different materials properties including DFT+U band gap opening in NiO, the relative stability of various polaron distributions in TiO₂, the dependence of the calculated TiO₂ band gap on +J corrections, and, finally, the role of the +U and +J corrections for the computed properties of a series of the hexahydrated transition metals. Our implementation provides results consistent with those already reported in the literature from comparable methods. We conclude the contribution with tests on the influence of the Löwdin orthonormalization on the occupancies, calculated parameters, and derived properties.

Keywords: DFT+U, linear response, CP2K, population analysis, subspace representation, polaron, fundamental gap, Hubbard U, Hund J, Kohn-Sham DFT

1. Introduction

Density Functional Theory (DFT)¹ is a formally exact theory. Still, its practical applications are based on approximations enabling the computation of the kinetic energy, exchange, and correlation contributions to the electronic DFT Hamiltonian^{2,3}. The Kohn-Sham formalism⁴ of DFT (KS-DFT), in combination with approximate exchange-correlation functionals, enables accurate prediction of many properties of systems of interest across the fields of physics, chemistry, material science, and biology in a parameter-free way⁵. Over the past few decades, KS-DFT has played a pivotal role in the simulation and understanding of many-atom systems^{6,7}.

However, the size of the models used in DFT calculations is often limited by the need to balance computational efficiency and cost, on the one hand, with the degree of similarity between the chosen model and the actual system under study, on the other. Too limited a model size may be problematic. For example, in modeling defective periodic systems, a too-small simulation cell results in constraints to the local electronic structure or geometry, which can cause DFT to incorrectly predict the properties of systems with long-range interactions and characteristics⁸. Also, for extended dense systems, such as liquids and solids, efficient DFT-based ab initio molecular dynamics are necessary for considering finite temperature effects⁵.

Among many academic and commercial software implementations of DFT, CP2K is a freely available and open-source package that can efficiently perform DFT calculations using a mixed Gaussian and plane-wave basis-set approach, allowing efficient large-scale AIMD simulations⁹. It uses an atom-centered Gaussian-type basis as the primitive basis to compact the wave function representation, making the Kohn-Sham Hamiltonian sparse. Conversely, an auxiliary plane-wave basis is used to describe the electronic density so that Fast Fourier Transforms (FFT) efficiency can be exploited to solve the Poisson equation and obtain the Hartree energy in a time that scales linearly with system size^{5,9,10}. Traditional approaches in CP2K to solve the self-consistent field (SCF) equations are $O(N^3)$. $O(N^3)$ DFT simulation by CP2K has been performed on systems up to $\sim 6 \times 10^3$ atoms. With newly developed algorithms, CP2K can perform $O(N)$ calculations for up to $\sim 1 \times 10^6$ atoms^{11,12}.

In addition to challenges in using DFT to simulate large-size systems, there are additional difficulties in applying it to simulate strongly correlated materials. The approximate local and semi-local exchange-correlation functionals widely used in the simulations of materials suffer, most notably, from the self-interaction error (SIE)¹³⁻¹⁷. The SIE manifests as a negative deviation, for fractional electron numbers, from the piece-wise linearity of the total energy as a function of the total number of electrons in the system¹⁸. This error causes an underestimation of the calculated electronic band gaps. It is understood to be a primary cause for the poor description by standard approximate functionals of the electronic states of materials containing d- or f-electrons, such as transition metal oxides¹⁹⁻²⁷. Over the years, a wide variety of approaches to remedy the SIE have been developed, such as hybrid DFT functionals, SIE-corrected DFT¹³, Fermi orbital SIE-corrections²⁸⁻³⁰, Koopman's compliant functionals^{31,32} as well as the use of beyond-DFT methods to correct for SIE-

related DFT deficiencies for instance, using the dynamical mean-field approach^{33–40} or the GW method^{41–44}, etc. Although these approaches, such as routinely-used hybrid DFT functionals, are becoming more affordable with current super-computer architectures, their still much higher computational costs compared with semi-local DFT continue to limit the size (or number) of the systems amenable to simulation at this level of theory. In addition, due to the incomplete removal of the SIE, and related systemic errors, by the addition of a fraction of Kohn-Sham exact exchange to an otherwise standard DFT functional, residual challenges remain for hybrid DFT in predicting the properties of some open-shell systems.^{45–47}

Among the most computationally favorable approaches to overcome the SIE limitation of DFT, Hubbard corrected DFT+U^{48–54,40} has emerged as a convenient, widely used method to partially correct the main quadratic component of the SIE^{55–57}. DFT+U presents the clear computational advantage of a cost slightly higher than standard KS DFT based on local and semi-local exchange-correlation functionals. The widely used rotational invariant, simplified DFT+U energy correction form is as follows^{58,48–50,54,59}:

$$E_U[\hat{n}^{I\sigma}] = \sum_{I\sigma} \frac{U^I}{2} \text{Tr}[\hat{n}^{I\sigma}(1 - \hat{n}^{I\sigma})]. \quad (1)$$

The DFT+U energy correction term is entirely determined by the occupation matrices $\hat{n}^{I\sigma}$ indexed by the Hubbard subspace I and spin channel σ , and the Hubbard U parameter U^I , which is an externally or first principles derived parameter that determines the extent of the energy correction.

In recent years, significant efforts and advances have taken place to extend and refine the DFT+U correction toward increased accuracy. The first strand of such advances stems from the idea that, in addition to the Hubbard U correction, the Hund's J correction for the intra-atom exchange (in the magnetics sense, and not to imply that it excludes correlation) can also be incorporated^{40,52,58,60–63}. Dudarev *et al.*⁵⁸ established the functional form in which the Hund's J correction can be introduced by adopting $U_{eff}^I = U^I - J^I$ as the parameter of like-spin correction in Eq. (1). Eq. (1) can also be extended to incorporate the unlike spin correction to become DFT+U+J^{40,52,61}. Himmetoglu *et al.*⁶¹ proposed a relatively new form of DFT+U+J correction. Ignoring the ‘minority term’ of Eq. (7) in Ref 61, as done there and in subsequent studies, the DFT+U+J energy correction term can be written as:

$$E_{U,J}[\hat{n}^{I\sigma}] = \sum_{I\sigma} \left\{ \frac{U^I - J^I}{2} \text{Tr}[\hat{n}^{I\sigma}(1 - \hat{n}^{I\sigma})] + \frac{J^I}{2} \text{Tr}[\hat{n}^{I\sigma}\hat{n}^{I-\sigma}] \right\}. \quad (2)$$

Where $-\sigma$ indicates the spin channel opposite to the σ one.

The second strand of improvements has focused on moving away from determining the U and J parameters semi-empirically towards calculating U and J parameters in a first-principles manner, as overviewed in Refs. 64 and 40. Initially, the Hubbard U parameters were obtained by aligning the results of DFT+U calculations with experimental data or higher-level computational results on the

spectral⁶⁵⁻⁶⁷, structural^{65,67,68}, or energy^{69,70}, etc. properties of the systems of interest. This method of determining the U parameter has some disadvantages. Rather than being an inherent property of the system, the U parameter is interpreted as an adjustable parameter. The U parameter is optimized so that DFT+U can accurately calculate certain specific properties of materials. However, this U parameter may not necessarily reflect the maximum degree of correction for the SIE, but rather is a product of various errors (including implementation details of DFT+U) canceling each other out. Therefore, using this parameter to compute other properties of materials may pose issues. In addition, there may be a lack of experimental data or higher-level computational results for relevant properties of the material of interest, which prevents tuning U corrections to reproduce such properties correctly.

Early attempts to calculate the U parameters from first principles relied on constrained LDA (cLDA)^{48,49,71-77}. This method decouples a given subspace, preventing electron-density transfer with other atoms in the simulation cell, thus neglecting screening effects between the subspace and the surrounding atoms. The U values calculated using this method are usually drastically overestimated. Constrained-RPA (cRPA)⁷⁸⁻⁸² is one of the more advanced U parameter calculation approaches. The method gives a fully frequency-dependent interaction parameter $U(\omega)$ that effectively accounts for the screening effect of electrons not in the subspace. However, it is computationally more expensive than the cLDA method, and incorporates elements that are extraneous to the underlying approximate density functional. Another popular option is the widely-used and successful linear-response method developed by Cococcioni et al. that can be used to calculate the U (as well as J, as of recently^{27,83}) parameter in Eq. (1)-(2) by finite difference⁵⁵. The method builds upon the earlier linear response scheme⁵⁴ proposed by Pickett et al. and shares many aspects of the modified constrained LDA⁸¹ proposed by Aryasetiawan et al.^{25,84}. Recently, the linear-response method for calculating the U parameter in Eq. (1)-(2) has been reformulated by Moynihan et al.⁸⁴ in terms of the constrained ground state density only, the so-called minimum-tracking linear response method, later expanded by Linscott et al.²⁵ towards the calculation of both the J parameter in Eq. (1)-(2) and spin-dependent U parameters. It has been recently shown that DFT+U+J with the corrective terms in Eq.(2) in combination with minimum tracking linear response Hubbard U and Hund's J parameters can provide accurate fundamental gaps for MnO²⁵ and TiO₂²⁶.

The third direction of contemporary DFT+U(+J) development has focused on identifying *appropriate* representations for the Hubbard subspaces. This area of work concerns reasonable forms of the Hubbard subspace occupation matrices, associated occupation numbers, and DFT+U+J corrective terms, e.g., DFT+U+J potential matrices and forces. Different approaches to projecting the KS states onto a set of localized orbitals referred to as "Hubbard projectors" result in different definitions of the Hubbard subspace and its occupation matrix in various DFT codes such as ONETEP⁸⁵, Siesta⁸⁶, OpenMX⁸⁷⁻⁹¹, Quantum ESPRESSO^{40,55,61,92,93}, VASP^{94,95}, ABINIT⁹⁶, FHI-aims⁹⁷, CONQUEST⁹⁸. One popular choice is to perform a Löwdin transformation for the density matrix (Kohn-Sham orbital expansion coefficient matrix) and the Kohn-Sham Hamiltonian matrix represented in the complete set of atom-centered, localized, and non-orthogonal basis functions. The projected sub-matrices corresponding to the sets of Hubbard projector functions (subsets of the

Löwdin transformed basis functions) are then extracted from the Löwdin transformed density matrix and Hamiltonian matrix^{99,40}. The Löwdin-transformed projector functions lose a certain degree of locality compared to the original basis functions. This is because the Löwdin-transformation mixes local basis functions centered on other atoms, especially if the basis set is one of the multiple-zeta type or contains many diffuse basis functions. Another option is using non-orthogonal Hubbard projectors and their duals to represent the correlated subspace appropriately. There are some early schemes, such as the "full" and "on-site"¹⁰⁰ representations, that are not tensorially consistent and result in a trace of the occupation matrix that is *not* equal to the number of electrons in the system when the Hubbard subspace is extended to the entire system^{87,101,102}. The "dual" representation⁸⁷ scheme, which utilizes the contravariant metric on the complete basis set in combination with symmetrization, provides a tensorially and physically meaningful trace. However, it also gives a physically meaningless matrix power^{101,102}. The "tensorial" representation proposed by O'Regan et al.¹⁰¹ and first implemented in ONETEP⁸⁵ utilizes the contravariant metric only on the subspace to construct projector duals. The "tensorial" representation results in occupancies that only accumulate contributions localized to the selected subspace. It can also automatically provide Hermitian DFT+U+J corrective energy, potential, and (real-valued) forces, which are physically meaningful and localized to the corresponding correlated subspace. By adopting the "tensorial" representation of the occupation matrix, the projector functions representing the Hubbard subspaces do not have to undergo any orthogonal transformation. They can retain more of their original local characteristics compared to approaches based on the Löwdin transformation scheme. In the "tensorial" representation, the occupation matrix is defined as:

$$\hat{n}^{I\sigma} = \hat{P}^I \hat{\rho}^\sigma \hat{P}^I, \quad (3)$$

where $\hat{\rho}^\sigma$ is the Kohn-Sham density operator. \hat{P}^I is the projection operator of subspace I , given by¹⁰¹

$$\hat{P}^I = \sum_m |\varphi^{Im}\rangle \langle \varphi_m^I|. \quad (4)$$

The projector functions φ_m^I s are usually atom-centered, fixed, spin-independent, localized, and orthonormal orbital functions. However, they can also be non-orthogonal¹⁰¹ and self-consistent¹⁰³. φ^{Im} is the projector function dual constructed concerning only the projector functions in the subspace I .

Recent years have also seen additional developments and theoretical extensions along the lines of the DFT+U approach, which we overview briefly and non-exhaustively due to space limitations. The DFT+U+V method¹⁰⁴ extends the on-site only DFT+U method by incorporating inter-site interaction terms. A recent reformulation of the linear response DFT method within density functional perturbation theory (DFPT) recasts the perturbation potential in the supercell as a sum of monochromatic perturbations in the primitive unit cell, achieving computationally convenient, automated calculations of the U and V parameters for selected atoms in a supercell^{104,105}. In the ACBN0 pseudo-hybrid Hubbard density functional approach the U and J parameters in the DFT+U corrected energy and potential are calculated directly as local Coulomb and exchange integrals, with screening effects approximated by involving the density matrix¹⁰⁶. Finally, several strategies for

self-consistency of the U , J , and V parameters have also been proposed and benchmarked in the specialized literature, also with attention to the balance between increased accuracy and computational overheads for automated applications^{56,104,61,107,84}.

All the advances mentioned above have sought to make DFT+ U approaches more accurate and less semi-empirical. In this context, this work aims to build on such advances, specifically, those focused on the simplified rotationally invariant DFT+ U and DFT+ U + J functionals, and make them usable for computationally efficient dynamic simulation (e.g., DFT molecular dynamics) for large and strongly correlated systems. To this end, we have implemented the DFT+ U + J (Equation 2) approach, an extended form of DFT+ U more elaborate than the “by-now conventional” one, into the Quickstep DFT code of the CP2K suite. The full analytical atomic forces contributed by the DFT+ U + J corrections based on the “tensorial” representation, which are necessary for geometry optimization and molecular dynamics, have also been derived and implemented in an efficient parallel way. The full analytical atomic forces contributed by the DFT+ U + J corrective energies based on the Löwdin representation have also been derived and then implemented in a numerical iterative manner. Lastly, the recently proposed minimum tracking linear response method has also been implemented to enable first principles calculation of U and J parameters, for both the “tensorial” and Löwdin representations. The results of all the new implementations have been benchmarked against recent results in the area. We have furthermore tested what Löwdin orthogonalization does to the occupancies, calculated parameters, and derived properties, in comparison to the results from the tensorial representation. The paper is organized as follows. In Sec. 2, we present the theoretical formalism of DFT+ U + J and its implementation details in the Quickstep DFT code of the CP2K suite, including atomic forces and the minimum tracking linear response method. In Sec. 3, we present the calculated results benchmarked against recent results in the area to validate our implementations. We summarize our work in Sec. 4.

2. Theory

In this section, we first derive the explicit formulas for the occupation matrix of a Hubbard subspace I (Section 2.1). We then derive the explicit formulas for the DFT+ U + J energy, potential, and force correction terms based on the “tensorial” representation of the projection operator¹⁰¹, which connect closely with their implementation details in CP2K⁵ (Section 2.2). In Section 2.3, we derive the DFT+ U + J energy, potential, and force correction terms based on the Löwdin representation. Finally, in Section 2.4, we derived the formulas needed for the minimum-tracking linear-response method in CP2K.

2.1. The “*tensorial*” population analysis within an expanded basis

To ensure transferability of the results and to limit computational overheads, the projector function for each Hubbard subspace is defined as a linear combination of the underlying basis functions⁹⁷ whose coefficients are predetermined by solving the pseudoatomic problem (ATOM code in CP2K) with a predefined total charge²⁶ in CP2K,

$$|\varphi_m^I\rangle = \sum_{\alpha} a^{I\alpha} |\phi_{m\alpha}^I\rangle. \quad (5)$$

$\phi_{m\alpha}^I$ is the basis function (contracted Gaussian function) centered on the atom (with subspace indexed I) with a specific angular momentum quantum number (which is not explicitly indicated here). m and α index the real spherical harmonics and radial part of the Gaussian functions, respectively. $a^{I\alpha}$ denotes the expansion coefficient for subspace I . In the ‘‘tensorial’’ representation, the dual projector function is defined as¹⁰¹

$$|\varphi^{Im}\rangle = \sum_{m' \in C^I} |\varphi_{m'}^I\rangle O^{Im'm}. \quad (6)$$

C^I denotes the set of spherical harmonic indices associated with subspace I being targeted for the DFT+U type correction. Then, the Hubbard projection operator in Eq. (4) is given by

$$\hat{P}^I = \sum_{m \in C^I} |\varphi^{Im}\rangle \langle \varphi_m^I| = \sum_{m, m' \in C^I} |\varphi_{m'}^I\rangle O^{Im'm} \langle \varphi_m^I|, \quad (7)$$

in which $O^{Im'm}$ is defined, and numerically evaluated in practice, as

$$O^{Im'm} = ((O_{co}^I)^{-1})^{m'm}, \quad (8)$$

and is obtained for each subspace I by a separate inverse operation of the ‘‘covariant’’ overlap matrix O_{co}^I of the Hubbard projector functions in the index set C^I ,

$$O_{m'm}^I = \langle \varphi_{m'}^I | \varphi_m^I \rangle = \sum_{\alpha'} \sum_{\alpha} a^{I\alpha'} a^{I\alpha} \langle \phi_{m'\alpha'}^I | \phi_{m\alpha}^I \rangle \equiv (O_{co}^I)_{m'm}. \quad (9)$$

Here, the subscript ‘‘co’’ is used only to indicate that O_{co}^I is a covariant-type matrix. One can then find that (the Einstein summation convention¹⁰⁸ is applied from here on, in which repeated indices inside the same expression are summed over unless the indices are enclosed in parenthesis)

$$O^{(I)mm'} O_{m'm''}^{(I)} = ((O_{co}^I)^{-1})^{mm'} (O_{co}^I)_{m'm''} = \delta_{m''}^m, \quad (10)$$

and

$$\langle \varphi_m^{(I)} | \varphi^{(I)m'} \rangle = \langle \varphi_m^{(I)} | \varphi_{m''}^{(I)} \rangle O^{(I)m''m'} = O_{mm''}^{(I)} O^{(I)m''m'} = \delta_m^{m'}. \quad (11)$$

The density operator corresponding to the spin channel of index σ is given by¹⁰

$$\hat{\rho}^{(\sigma)} = \sum_i |\psi_i^{(\sigma)}\rangle f_i^{(\sigma)} \langle \psi_i^{(\sigma)}|, \quad (12)$$

where $f_i^{(\sigma)}$ is the occupancy of the Kohn-Sham orbital $\psi_i^{(\sigma)}$. In combination with Eq. (3)-(12), and considering that CP2K uses real basis functions and the represented Kohn-Sham orbitals are real functions, the occupation matrix with one raised (m') and one lowered (m) index for each subspace¹⁰¹ is given by

$$\begin{aligned}
n_m^{(I)(\sigma)m'} &= \langle \varphi_m^{(I)} | \hat{\rho}^{(\sigma)} | \varphi^{(I)m'} \rangle \\
&= \langle \varphi_m^{(I)} | \psi_i^{(\sigma)} \rangle f_i^{(\sigma)} \langle \psi_i^{(\sigma)} | \varphi^{(I)m'} \rangle \\
&= \langle \varphi_m^{(I)} | \psi_i^{(\sigma)} \rangle f_i^{(\sigma)} \langle \psi_i^{(\sigma)} | \varphi_{m''}^{(I)} \rangle \mathcal{O}^{(I)m''m'} \\
&= a^{(I)\alpha'} \langle \phi_{m\alpha'}^{(I)} | \psi_i^{(\sigma)} \rangle f_i^{(\sigma)} \langle \psi_i^{(\sigma)} | \phi_{m''\alpha}^{(I)} \rangle a^{(I)\alpha} \mathcal{O}^{(I)m''m'} \\
&= a^{(I)\alpha'} \langle \phi_{m\alpha'}^{(I)} | \phi_\beta \rangle \langle \phi_\beta | \psi_i^{(\sigma)} \rangle f_i^{(\sigma)} \\
&\quad \langle \psi_i^{(\sigma)} | \phi_\gamma \rangle \langle \phi_\gamma | \phi_{m''\alpha}^{(I)} \rangle a^{(I)\alpha} \mathcal{O}^{(I)m''m'} \\
&= a^{(I)\alpha'} S_{(I)m\alpha',\beta} C_{(\sigma)i}^\beta f_i^{(\sigma)} (C^T)_{(\sigma)i}^\gamma S_{\gamma,(I)m''\alpha} a^{(I)\alpha} \mathcal{O}^{(I)m''m'} \\
&= a^{(I)\alpha'} S_{(I)m\alpha',\beta} D^{(\sigma)\beta\gamma} S_{\gamma,(I)m''\alpha} a^{(I)\alpha} \mathcal{O}^{(I)m''m'} \\
&= a^{(I)\alpha'} a^{(I)\alpha} D_{m\alpha',m''\alpha}^{(I)(\sigma)} \mathcal{O}^{(I)m''m'}. \tag{13}
\end{aligned}$$

The ϕ_β (or the one indexed by the other Greek letters) is a contracted Gaussian basis function within the simulation cell, where β (or other Greek letters) traverses all the contracted Gaussian basis functions. ϕ^β is the dual function of ϕ_β which is defined as $|\phi^\beta\rangle = |\phi_\beta\rangle(S^{-1})^{\gamma\beta}$. In CP2K, $D^{(\sigma)\beta\gamma} = C_{(\sigma)i}^\beta f_i^{(\sigma)} (C^T)_{(\sigma)i}^\gamma$ is the matrix element of the contravariant density matrix based on the contracted Gaussian basis functions. S is the overlap matrix. C is the coefficient matrix, whose columns contain the expansion coefficients of a Kohn-Sham orbital in the adopted Gaussian basis functions⁵.

2.2 DFT+U+J energy, potential and force in the “tensorial” representation

In combination with the analytical form of the occupation matrix in Eq. (13), the DFT+U+J energy (Eq. (2)) can be rewritten as

$$E_{U,J} = \frac{1}{2} \sum_{I\sigma} (U^{(I)} - J^{(I)}) (Tr[n^{(I)(\sigma)}] - Tr[n^{(I)(\sigma)} n^{(I)(\sigma)}]) + \frac{1}{2} \sum_{I\sigma} J^{(I)} Tr[n^{(I)(\sigma)} n^{(I)(-\sigma)}]. \tag{14}$$

Before deriving subspace- I resolved formulas for the DFT+U+J corrective potential matrix and DFT+U+J analytical forces, let us define the overlap between a basis function and a given projector function as

$$V_{\beta m}^{(I)} \equiv \langle \phi_\beta | \varphi_m^{(I)} \rangle = \langle \phi_\beta | \phi_{m\alpha}^{(I)} \rangle a^{(I)\alpha}, \tag{15}$$

$$W_{m\gamma}^{(I)} \equiv \langle \varphi_m^{(I)} | \phi_\gamma \rangle = a^{(I)\alpha*} \langle \phi_{m\alpha}^{(I)} | \phi_\gamma \rangle, \quad (16)$$

and the full matrix $P^{(I)}$ as

$$\begin{aligned} P_{\beta\gamma}^{(I)} &\equiv V_{\beta m'}^{(I)} O^{(I)m'm} W_{m\gamma}^{(I)} \\ &= \langle \phi_\beta | \phi_{m'\alpha'}^{(I)} \rangle a^{(I)\alpha'} O^{(I)m'm} a^{(I)\alpha*} \langle \phi_{m\alpha}^{(I)} | \phi_\gamma \rangle \\ &= S_{\beta,(I)m'\alpha'} a^{(I)\alpha'} O^{(I)m'm} a^{(I)\alpha*} S_{(I)m\alpha,\gamma}. \end{aligned} \quad (17)$$

In combination with the expression of $n_m^{(I)(\sigma)m'}$, we can reformulate $n_m^{(I)(\sigma)m'}$ as

$$n_m^{(I)(\sigma)m'} = W_{m\beta}^{(I)} D^{(\sigma)\beta\gamma} V_{\gamma m''}^{(I)} O^{(I)m''m'} = [W^{(I)} D^{(\sigma)} V^{(I)} O^{(I)}]_m^{m'}. \quad (18)$$

Next, the DFT+U+J energy in Eq. (14) can be rewritten as

$$\begin{aligned} E_{U,J} &= \frac{1}{2} \sum_{I\sigma} (U^{(I)} - J^{(I)}) (\text{Tr}[P^{(I)} D^{(\sigma)}] - \text{Tr}[P^{(I)} D^{(\sigma)} P^{(I)} D^{(\sigma)}]) \\ &\quad + \frac{1}{2} \sum_{I\sigma} J^{(I)} \text{Tr}[P^{(I)} D^{(\sigma)} P^{(I)} D^{(-\sigma)}]. \end{aligned} \quad (19)$$

The contribution of the DFT+U+J potential to the Kohn-Sham Hamiltonian matrix is given by the partial derivative of the DFT+U+J energy terms in Eq. (19) with respect to the density matrix elements⁵. The matrix elements of the DFT+U+J potential are given by (the complete derivation is provided in Section 1 of the Supporting Information)

$$\begin{aligned} (H^{U,J})_{\beta\gamma}^\sigma &= \frac{\partial E_{U,J}}{\partial D^{(\sigma)\gamma\beta}} \\ &= \sum_I S_{\beta,(I)ba'} a^{(I)\alpha'} O^{(I)ba} \left\{ \frac{U^{(I)} - J^{(I)}}{2} \cdot [\delta_d^c - 2 \cdot n_d^{(I)(\sigma)c}] + J^{(I)} n_d^{(I)(-\sigma)c} \right\} a^{(I)\alpha*} S_{(I)ca,\gamma}. \end{aligned} \quad (20)$$

The DFT+U+J contribution to the force on the I is given by

$$\vec{F}_{R_k}^{U,J} = - \frac{\partial E_{U,J}}{\partial R_k^{aI}} = - \sum_{I'} \frac{\partial E_{U,J}}{\partial P_{\beta\gamma}^{(I')}} \frac{\partial P_{\beta\gamma}^{(I')}}{\partial R_k^{aI}} - \sum_{\sigma} \frac{\partial E_{U,J}}{\partial D^{(\sigma)\kappa\lambda}} \frac{\partial D^{(\sigma)\kappa\lambda}}{\partial R_k^{aI}} = \vec{F}_{P,R_k}^{U,J} + \vec{F}_{D,R_k}^{U,J}. \quad (21)$$

where $\overrightarrow{R_k^{aI}}$ denotes one of the three Cartesian components ($k = x, y, \text{ or } z$) of the position vector for the atom at which subspace I is hosted. aI denotes the index of that atom. The first and second summation terms in Eq. (21) are indicated as $\vec{F}_{P,R_k}^{U,J}$ and $\vec{F}_{D,R_k}^{U,J}$, respectively. P and D in the subscripts denote that the derivative terms involve matrix elements of the $P^{(I)}$ and $D^{(\sigma)}$ matrix, respectively. The forces are calculated upon convergence of the energy minimization procedure for

the electronic structure of the given ionic configuration. The term $\vec{F}_{D,R_k}^{U,J}$ arises from the terms in Eq. 20 and the derivatives of the density matrix elements with respect to the atom coordinate. It can be calculated directly from the energy weighted density matrix and the first derivatives of the overlap matrix with respect to the atomic coordinates⁵. As a result, we only need to explicitly consider and implement the missing $\vec{F}_{P,R_k}^{U,J}$ term.

From the expression of $\vec{F}_{P,R_k}^{U,J}$ given in Eq. (21) and Eq. (19), one can derive (the full derivation is provided in Section 2 of the Supporting Information)

$$\frac{\partial E_{U,J}}{\partial P_{\beta\gamma}^{(I')}} = \frac{1}{2} \sum_{\sigma} \left[(U^{(I')} - J^{(I')}) \left(D^{(\sigma)\gamma\beta} - 2 \cdot D^{(\sigma)\gamma\epsilon} P_{\epsilon I}^{(I')} D^{(\sigma)\epsilon\beta} \right) + J^{(I')} \left(2 \cdot D^{(\sigma)\gamma\pi} P_{\pi\rho}^{(I')} D^{(-\sigma)\rho\beta} \right) \right]. \quad (22)$$

Considering Eqs. (15)-(17) and that our basis functions are real functions, one then obtains

$$\begin{aligned} \frac{\partial P_{\beta\gamma}^{(I')}}{\partial R_k^{ai_i}} &= \frac{\partial \left(S_{\beta,(I')m'\alpha'} a_{\alpha'}^{(I')} O^{(I')m'm} a_{\alpha}^{(I')*} S_{(I')m\alpha,\gamma} \right)}{\partial R_k^{ai_i}} \\ &= \frac{\partial \left(S_{\beta,(I')m'\alpha'} \right)}{\partial R_k^{ai_i}} a^{(I')\alpha'} O^{(I')m'm} W_{m\gamma}^{(I')} + V_{\beta m'}^{(I')} O^{(I')m'm} a^{(I')\alpha*} \frac{\partial \left(S_{(I')m\alpha,\gamma} \right)}{\partial R_k^{ai_i}}. \end{aligned} \quad (23)$$

Let us denote the x, y, and z components of the first derivative of the overlap matrix element $\langle \phi_{\beta} | \phi_{\gamma} \rangle$ with respect to the position of the basis function ϕ_{β} 's center as $G_{\beta\gamma}^i$ ($i = x, y, z$). The G^i matrices for the x, y, and z directions are from the original environment of Quickstep in CP2K. The index of the atom the basis function ϕ_{β} is centered at is denoted as $ai_{\phi_{\beta}}$. Given the relation of $G_{\beta\gamma}^i = -G_{\gamma\beta}^i$ and Eq. (23), one then obtains (the complete derivation is provided in Section 3 of the Supporting Information)

$$\begin{aligned} \frac{\partial P_{\beta\gamma}^{(I')}}{\partial R_k^{ai_i}} &= L_{\beta,(I')m'}^{k,I} O^{(I')m'm} W_{m\gamma}^{(I')} + V_{\beta m'}^{(I')} O^{(I')m'm} \left(L_{(I')m,\gamma}^{k,I} \right)^* \\ &= \left[\left(L^{k,I} O^{(I')} W^{(I')} \right) + \left(L^{k,I} O^{(I')} W^{(I')} \right)^{\dagger} \right]_{\beta\gamma}. \end{aligned} \quad (24)$$

Where $L_{\beta,(I')m'}^{k,I}$ is defined as

$$L_{\beta,(I')m'}^{k,I} = \left(\delta_{ai_{\phi_{\beta}} ai_i} G_{\beta,(I')m'\alpha'}^k - G_{\beta,(I')m'\alpha'}^k \delta_{ai_i, ai_i} \right) a^{(I')\alpha'}. \quad (25)$$

Combining Eqs. (21), (22), and (24), we arrive at the final form of $\vec{F}_{P,R_k}^{U,J}$, given by

$$\begin{aligned}
\hat{F}_{P,R_k}^{U,J} &= - \sum_{I'} \frac{\partial E_{U,J}}{\partial P_{\beta\gamma}^{(I')}} \frac{\partial P_{\beta\gamma}^{(I')}}{\partial R_k^{a_i}} \\
&= - \sum_{I'} \left\{ \sum_{\sigma} \left[\frac{1}{2} (U^{(I')} - J^{(I')}) (D^{(\sigma)} - 2 \cdot D^{(\sigma)} P^{(I')} D^{(\sigma)}) + J^{(I')} (D^{(\sigma)} P^{(I')} D^{(-\sigma)}) \right] \right\}^{\nu\beta} \\
&\quad \left[(L^{k,I} O^{(I')} W^{(I')}) + (L^{k,I} O^{(I')} W^{(I')})^\dagger \right]_{\beta\gamma} . \quad (26)
\end{aligned}$$

2.3 DFT+U+J within the Löwdin representation

Since 2008, there have been DFT+U implementations in CP2K based on Löwdin charges (representation), Mulliken population analysis, and Mulliken charges¹⁰⁹. The current DFT+U implementation based on the Löwdin representation is discussed in this part in an operator-language fashion so as to derive the analytical formulas of the contributed analytical forces and the fundamental quantities used in the minimum-tracking linear response method. In the implementation of DFT+U based on the Löwdin representation⁹⁹ in CP2K, the projection operator is defined as

$$\hat{P}^I = \sum_{m\alpha} |\bar{\phi}_{(I)m\alpha}\rangle \langle \bar{\phi}_{(I)m\alpha}|, \quad (27)$$

in which the projector is defined as

$$|\bar{\phi}_{(I)m\alpha}\rangle = |\phi_\gamma\rangle \left(S^{-\frac{1}{2}} \right)_{\gamma,(I)m\alpha}. \quad (28)$$

$|\bar{\phi}_{(I)m\alpha}\rangle$ is the Löwdin transformed basis function for subspace I , centered at atom a_i . The spherical harmonic is indexed by m and the radial function is indexed by α . S is the overlap matrix for the set of all the basis functions in the simulation cell. These Löwdin transformed basis functions are orthogonal to each other. For the simplicity of notations, we label $S^{\frac{1}{2}}$ as A

$$A \equiv S^{\frac{1}{2}}. \quad (29)$$

From Eqs. (3), (27), and (28), the occupation matrix of the subspace I is given by (see Section 4 in the Supporting Information for the complete derivation),

$$\tilde{n}_{m\alpha,m'\alpha'}^{(I)(\sigma)} = (A D^{(\sigma)} A)_{(I)m\alpha,(I)m'\alpha'}. \quad (30)$$

For the present work, we have additionally introduced the correction terms of the +J energy and potential into the existing implementation of the +U energy and potential corrections for the Löwdin DFT+U method in CP2K. Based on the energy expression in Eq. (2) and the analytical form of the occupation matrix in Eq. (30), the DFT+U+J energy including the +J correction can then be written as

$$\begin{aligned}
E_{U,J} = & \frac{1}{2} \sum_{I\sigma} (U^{(I)} - J^{(I)}) \left((AD^{(\sigma)}A)_{(I)m\alpha,(I)m\alpha} \right. \\
& - (AD^{(\sigma)}A)_{(I)m'\alpha',(I)m''\alpha''} (AD^{(\sigma)}A)_{(I)m''\alpha'',(I)m'\alpha'} \\
& \left. + \frac{1}{2} \sum_{I\sigma} J^{(I)} (AD^{(\sigma)}A)_{(I)m'''\alpha''',(I)m''''\alpha''''} (AD^{(-\sigma)}A)_{(I)m''''\alpha'''',(I)m'''\alpha'''} \right). \quad (31)
\end{aligned}$$

To derive the +J corrective potential, one should derive the derivative of the correction energy with respect to the density matrix elements. The potential of the +J correction (the potential of the +U correction was already present in the pre-existing Löwdin DFT+U implementation in CP2K) to be added to the overall Kohn-Sham Hamiltonian is given by (the second summation term is denoted as E_J in the complete derivation provided in Section 5 in the Supporting Information),

$$(H^J)_{\beta\gamma}^\sigma = \sum_I J^{(I)} A_{\beta,(I)m'\alpha'} \bar{n}_{m'\alpha',m\alpha}^{(I)(-\sigma)} A_{(I)m\alpha,\gamma}. \quad (32)$$

The DFT+U+J contribution to the force on the ion ai_l is given by

$$\vec{F}_{R_k^{ai_l}}^{U,J} = - \frac{\partial E_{U,J}}{\partial R_k^{ai_l}} = - \frac{\partial E_{U,J}}{\partial A_{\beta\gamma}} \frac{\partial A_{\beta\gamma}}{\partial R_k^{ai_l}} - \sum_{\sigma} \frac{\partial E_{U,J}}{\partial D^{(\sigma)\kappa\lambda}} \frac{\partial D^{(\sigma)\kappa\lambda}}{\partial R_k^{ai_l}} = \vec{F}_{P,R_k^{ai_l}}^{U,J} + \vec{F}_{D,R_k^{ai_l}}^{U,J}. \quad (33)$$

The first and second summation terms in Eq. (33) are denoted as $\vec{F}_{P,R_k^{ai_l}}^{U,J}$ and $\vec{F}_{D,R_k^{ai_l}}^{U,J}$, respectively. In

this case, as same as in the case of the “tensorial” representation, we need to add and implement the $\vec{F}_{P,R_k^{ai_l}}^{U,J}$ contribution explicitly. With $gl((I)m\alpha)$ denoting the global index of the joint indexes

$'(I)m\alpha'$ in the rows or columns of the A matrix, and based on Eq. (32), $\frac{\partial E_{U,J}}{\partial A_{\beta\gamma}}$ can be written as (see

Section 6 in the Supporting Information for the complete derivation)

$$\begin{aligned}
\frac{\partial E_{U,J}}{\partial A_{\beta\gamma}} = & \frac{1}{2} \sum_{I\sigma} (U^{(I)} - J^{(I)}) \left(\begin{aligned} & (K_{(I)m\alpha}^{(\sigma)\gamma} - 2 \cdot K_{(I)m'\alpha'}^{(\sigma)\gamma} A_{(I)m'\alpha',\mu} K_{(I)m\alpha}^{(\sigma)\mu}) \delta_{\beta}^{gl((I)m\alpha)} \\ & + \delta_{\gamma}^{gl((I)m\alpha)} \left(\left((K^{(\sigma)})^T \right)_{(I)m\alpha}^{\beta} - 2 \cdot \left((K^{(\sigma)})^T \right)_{(I)m\alpha}^{\nu} A_{\nu,(I)m'\alpha'} \left((K^{(\sigma)})^T \right)_{(I)m'\alpha'}^{\beta} \right) \end{aligned} \right) \\
& + \frac{1}{2} \sum_{I\sigma} J^{(I)} \left(\begin{aligned} & 2 \cdot K_{(I)m'''\alpha'''}^{(\sigma)\gamma} A_{(I)m'''\alpha''',\iota} K_{(I)m'''\alpha''',\sigma}^{(-\sigma)\iota} \delta_{\beta}^{gl((I)m'''\alpha''')} \\ & + 2 \cdot \delta_{\gamma}^{gl((I)m'''\alpha''')} \left((K^{(\sigma)})^T \right)_{(I)m'''\alpha'''}^{\sigma} A_{\sigma,(I)m'''\alpha'''} \left((K^{(-\sigma)})^T \right)_{(I)m'''\alpha'''}^{\beta} \end{aligned} \right), \quad (34)
\end{aligned}$$

in which

$$K_{(I)m\alpha}^{(\sigma)\gamma} \equiv (D^{(\sigma)})^{\gamma\lambda} A_{\lambda,(I)m\alpha}. \quad (35)$$

The term $\frac{\partial A_{\beta\gamma}}{\partial R_k^{ai_l}}$ in Eq. (33) can be instead written as

$$\frac{\partial A_{\beta\gamma}}{\partial R_k^{a_I}} = \frac{\partial \left(S^{\frac{1}{2}} \right)_{\beta\gamma}}{\partial R_k^{a_I}}, \quad (36)$$

and obtained by solving the equation

$$\frac{\partial (S)_{\beta\alpha}}{\partial R_k^{a_I}} = \frac{\partial \left(S^{\frac{1}{2}} \right)_{\beta\gamma}}{\partial R_k^{a_I}} \left(S^{\frac{1}{2}} \right)_{\gamma\alpha} + \left(S^{\frac{1}{2}} \right)_{\beta\gamma} \frac{\partial \left(S^{\frac{1}{2}} \right)_{\gamma\alpha}}{\partial R_k^{a_I}}. \quad (37)$$

The equation can be solved numerically via an iterative procedure and the subroutine is available in CP2K. The generalized Riccati or Sylvester equation in CP2K can be solved by using the preconditioned conjugate gradient algorithm, and we are now utilizing it to solve Eq (37)¹¹⁰.

2.4 Minimum-tracking linear-response method for calculating Hubbard U and Hund's J parameters in CP2K

In the minimum-tracking linear response method, the U (and J) parameters are defined based on the changes in *a*) the occupancy and *b*) the subspace-averaged Hartree + xc potential for subspace *I* and spin channel σ . The external potential that induces changes in the occupation of the subspace *I* in spin channel σ is given by^{25,55,64,84}

$$\hat{v}_{ext}^{(I)(\sigma)} = \omega^{(\sigma)} \hat{P}^{(I)}. \quad (38)$$

In practice, for the given site *I* and spin σ , an external perturbative potential is added to the Kohn-Sham matrix

$$H_{\beta\gamma}^{(I)(\sigma)\omega} = \langle \varphi_\beta | \hat{v}_{ext}^{(I)(\sigma)} | \varphi_\gamma \rangle = \omega^{(\sigma)} \langle \varphi_\beta | \hat{P}^{(I)} | \varphi_\gamma \rangle. \quad (39)$$

For the ‘‘tensorial’’ representation case, in combination with Eqs. (7) and (17), we obtain

$$H_{\beta\gamma}^{(I)(\sigma)\omega, \text{‘‘tensorial’’}} = \omega^{(\sigma)} V_{\beta m'}^{(I)} O^{(I)m'm} W_{m\gamma}^{(I)} = \omega^{(\sigma)} P_{\beta\gamma}^{(I)}. \quad (40)$$

For the Löwdin case, in combination with Eqs. (27) and (28), we have

$$H_{\beta\gamma}^{(I)(\sigma)\omega, \text{‘‘Lowdin’’}} = \omega^{(\sigma)} \left(S^{\frac{1}{2}} \right)_{\beta, (I)m\alpha} \left(S^{\frac{1}{2}} \right)_{(I)m\alpha, \gamma}. \quad (41)$$

With the application of the external perturbing potential of a given strength, at the end of the energy minimization procedure, the subspace-averaged occupation number of the subspace *I* is calculated as the trace of occupation matrix $n^{(I)(\sigma)}$ in Eq. (13)

$$N^{(I)(\sigma)} = Tr[n^{(I)(\sigma)}] = \sum_m n_{(m)}^{(I)(\sigma)(m)}, \quad (42)$$

for the ‘‘tensorial’’ representation case, and the one of occupation matrix $\bar{n}^{(I)(\sigma)}$ in Eq. (30)

$$\bar{N}^{(I)(\sigma)} = \text{Tr}[\bar{n}^{(I)(\sigma)}] = \sum_{m\alpha} \bar{n}_{(m)(\alpha)}^{(I)(\sigma)(m)(\alpha)}, \quad (43)$$

for the Löwdin case. The subspace-averaged Hartree + xc potential, as in Refs. ^{64,84}, is defined as

$$\frac{\text{Tr}[\hat{V}_{Hxc}^{(\sigma)} \hat{P}^{(I)}]}{\text{Tr}[\hat{P}^{(I)}]}. \quad (44)$$

For the “tensorial” representation case, in combination with Eq. (7), we have (see Section 7 in the Supporting Information for the complete derivation)

$$V_{Hxc}^{(I)(\sigma)} \equiv \frac{\text{Tr}[\hat{V}_{Hxc}^{(\sigma)} \hat{P}^{(I)}]}{\text{Tr}[\hat{P}^{(I)}]} = \frac{a^{(I)\alpha*} (V_{Hxc}^{(\sigma)})_{(I)m\alpha, (I)m'\alpha'} a^{(I)\alpha' *} O^{(I)m'm}}{a^{(I)\alpha''*} a^{(I)\alpha''' } S_{(I)m''\alpha'', (I)m'''\alpha'''} O^{(I)m''m''}}. \quad (45)$$

Given the relation in Eq. (9), Eq. (45) can be rewritten as

$$V_{Hxc}^{(I)(\sigma)} = \frac{a^{(I)\alpha*} (V_{Hxc}^{(\sigma)})_{(I)m\alpha, (I)m'\alpha'} a^{(I)\alpha' } O^{(I)m'm}}{O_{m''m'''}^{(I)} O^{(I)m''m''}} = \frac{a^{(I)\alpha*} (V_{Hxc}^{(\sigma)})_{(I)m\alpha, (I)m'\alpha'} a^{(I)\alpha' } O^{(I)m'm}}{|\{m\}^{(I)}|}. \quad (46)$$

$V_{Hxc}^{(\sigma)}$ is the Hartree + exchange-correlation matrix for spin σ , and the γ index runs over all the basis functions in the simulation cell. $\phi^{(\gamma)}$ is the global dual of basis function $\phi_{(\gamma)}$

$$|\phi^{(\gamma)}\rangle = |\phi_t\rangle (S^{-1})^{t(\gamma)}. \quad (47)$$

For the Löwdin case, in combination with Eqs. (27), (28), and (44), we have (see Section 7 in the Supporting Information for the full derivation)

$$\bar{V}_{Hxc}^{(I)(\sigma)} = \frac{\sum_{m\alpha} \left(S^{-\frac{1}{2}} V_{Hxc}^{(\sigma)} S^{-\frac{1}{2}} \right)_{(I)(m)(\alpha), (I)(m)(\alpha)}}{|\{m'\}^{(I)}| \cdot |\{\alpha'\}^{(I)}|}. \quad (48)$$

In this work, we have implemented only the “scaled 2×2” approach, which is entirely equivalent to the spin-independent (spins perturbed and monitored together) linear response method of calculating the Hubbard U, but is more general than the conventional linear response in terms of its capacity to calculate the Hund’s J too. In this approach, the U (J) parameter is the positive (negative) rate of change of spin-averaged sum (difference) of subspace-averaged Hartree-plus-exchange-correlation interaction with respect to sum (difference) of the occupation number of the subspace. The linear response U and J parameters in the “tensorial” representation are given by

$$U^{(I)} = \frac{1}{2} \frac{d \left(V_{Hxc}^{(I)(\uparrow)} + V_{Hxc}^{(I)(\downarrow)} \right)}{d(N^{(I)(\uparrow)} + N^{(I)(\downarrow)}),} \quad (49)$$

and, nothing the additional global minus sign,

$$J^{(I)} = -\frac{1}{2} \frac{d \left(V_{Hxc}^{(I)(\uparrow)} - V_{Hxc}^{(I)(\downarrow)} \right)}{d \left(N^{(I)(\uparrow)} - N^{(I)(\downarrow)} \right)}. \quad (50)$$

The ones in the Löwdin representation are given by

$$U^{(I)} = \frac{1}{2} \frac{d \left(\bar{V}_{Hxc}^{(I)(\uparrow)} + \bar{V}_{Hxc}^{(I)(\downarrow)} \right)}{d \left(\bar{N}^{(I)(\uparrow)} + \bar{N}^{(I)(\downarrow)} \right)}, \quad (51)$$

and

$$J^{(I)} = -\frac{1}{2} \frac{d \left(\bar{V}_{Hxc}^{(I)(\uparrow)} - \bar{V}_{Hxc}^{(I)(\downarrow)} \right)}{d \left(\bar{N}^{(I)(\uparrow)} - \bar{N}^{(I)(\downarrow)} \right)}. \quad (52)$$

In practice, in a modification to the “scaled 2×2” approach used in the present work, to simultaneously calculate the U and J parameters of a selected subspace I , we add to the Kohn-Sham Hamiltonian a perturbative potential, $\hat{v}_{ext}^{(I)(\sigma)}$ in Eq. (38) whose perturbation strength ω is given by

$$\omega^{(\uparrow)} = \delta V_{ext} - 0.1 \cdot \delta V_{ext}, \quad (53)$$

for the spin α denoted as (\uparrow) and another one

$$\omega^{(\downarrow)} = \delta V_{ext} + 0.1 \cdot \delta V_{ext}, \quad (54)$$

for the spin β denoted as (\downarrow). δV_{ext} s are selected as small values around zero, such as

$$\delta V_{ext} \in \{-0.2, -0.1, 0.0, 0.1, 0.2\} \text{ (Unit: eV)}.$$

The subspace occupancy $N^{(I)(\sigma)}$ or $\bar{N}^{(I)(\sigma)}$ and the subspace averaged Hartree + XC potential $V_{Hxc}^{(I)(\sigma)}$ or $\bar{V}_{Hxc}^{(I)(\sigma)}$ are then calculated from the perturbed ground state electronic structure. By changing the δV_{ext} values, the $U^{(I)}$ and $J^{(I)}$ parameters can then be calculated by using a finite difference approach.

3. Results and discussions

This Section presents our benchmarking of a) the DFT+U+J implementation (including corrective energy, potential, and force terms for +U and +J corrections) in CP2K based on the "tensorial" representation, b) the +J extension of the existing DFT+U implementations based on the Löwdin representation in CP2K (including +J corrective energy and potential, and forces introduced by both U and J corrections), and c) the implementation of the minimum tracking linear response method in CP2K. We first present and discuss the results for the band gap of NiO (Section 3.1) and polaron distribution at a reduced TiO₂ surface (Section 3.2) calculated using DFT+U for the "tensorial" representation. Next, we focus on the results for the unlike-spin +J correction term and the linear response U and J parameters in "tensorial" and Löwdin representations. The benchmarks for DFT+U+J with first-principles linear response U and J parameters have been carried out on the

bulk TiO₂ band gap (Section 3.3). The benchmark for the calculated linear response U and J values have instead been performed considering a series of transition metal hexahydrates (Section 3.4). We conclude the section by presenting a benchmark comparison of our DFT+U+J force implementation for the "tensorial" and Löwdin cases (section 3.5).

3.1. DFT+U band gap opening in NiO

We first calculated the variation of the NiO band gap with the applied U correction using our implementation of DFT+U in the "tensorial" representation and compared the results with available calculations from the literature. As widely documented^{111–114,55}, NiO's partially filled *d* orbitals lead to spectacular accuracy failures for Kohn-Sham DFT based on approximated local and semi-local exchange-correlation functionals. As a result, and given the abundance of high-level experimental results, NiO has been extensively used as a validation system for beyond-DFT approaches such as DFT+U^{55,87,95,97,99,101,115–117}, SIC-LDA^{111,118,119}, GW approximations^{120–123}, and DFT+DMFT^{124–130}. NiO is an antiferromagnetic rock-salt structure insulator¹³¹ with an insulating gap of O *2p*→Ni *3d* charge transfer type¹³². Local and semi-local exchange-correlation functionals severely underestimate the band gap and local magnetic moments and predict a valence band edge of mainly Ni *3d* character with negligible O *2p* contributions^{113,133,95,55,96,97}. The literature has extensively reported that DFT+U can correct the shortcomings of standard (local and semi-local) DFT and reproduce the main physical features of NiO^{50,58,95,55,96,97,101}. We accordingly focused on NiO as the first test system to validate our implementation of the "tensorial" DFT+U method for correlated transition metal oxides.

We first optimized bulk NiO's geometry and cell parameters with the Perdew-Burke-Ernzerhof (PBE) exchange-correlation functional¹³⁴ in CP2K. We then performed a set of single-point energy calculations on the PBE-optimized geometry using the newly implemented "tensorial" DFT+U in CP2K. The U corrections were only applied to the Ni *3d* states. The predetermined projector functions used in these calculations were obtained by solving the Ni +0 pseudo-atom problem by using the ATOM program in CP2K. Fig. 1 reports the band gaps and the projected density of states calculated with different U values.

As shown in Fig. 1, the calculated Kohn-Sham band-gap increases with the U parameter due to the expected downward and upward shifts, respectively, of occupied and unoccupied *d*-orbitals⁴⁰. Since the PBE functional wrongly predicts a dominant Ni *3d* character for the valence band maximum (VBM) and conduction band minimum (CBM), and the U corrections were only applied to Ni *3d* orbitals, the simulations result in the expected linear dependence of the (*d*) band-gap on the applied U values⁹⁷. Notably, and different from some results in the literature⁹⁷, the linear behavior of the (*3d*) band-gap versus the U value is not disrupted in the large U region. In our simulations, the O *p*, Ni *s*, and O *s* bands around the VBM and CBM are almost unaffected by applying the U correction to the Ni *3d* states owing to the limited hybridization between these states and the U-corrected Ni *3d* states. The difference between the "tensorial" and "dual" representations, the latter of which was employed in the calculations in Ref. ⁹⁷ and needs the inverse of the overlap matrix of all the basis functions in the simulation cell to form the Hubbard projector dual, might be the source

of this discrepancy^{87,101}. Even if the Ni 3d gap is considerably widened for U values greater than 6 eV, the predicted VBM and CBM are now due to O p, O s, and Ni s bands, so the calculated band gap saturates.

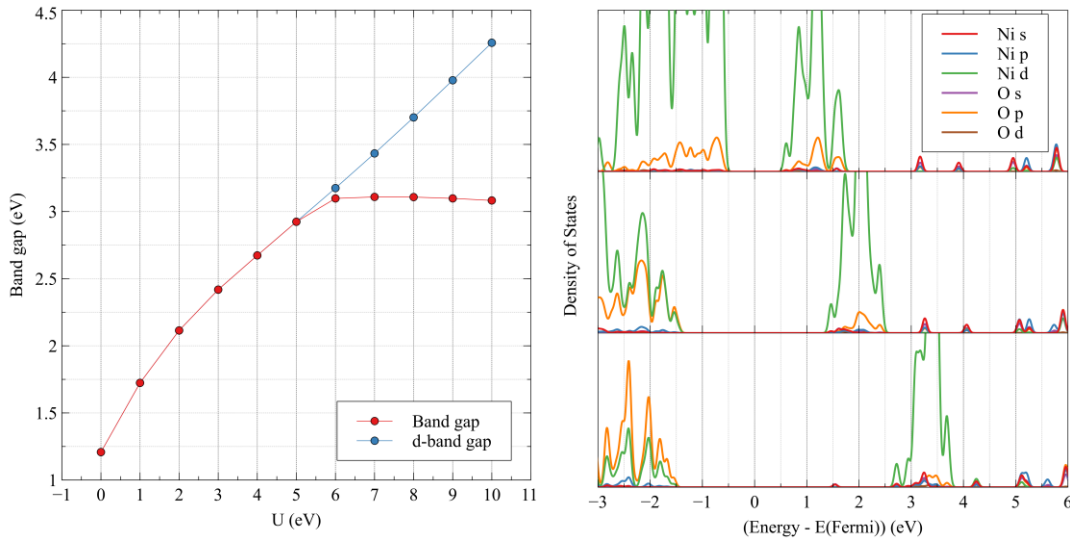


Figure. 1 (Left panel) The calculated (generalized) Kohn-Sham band gap (red) and d-band gap (blue) of NiO as a function of the U values. (Right panel) Atom- and angular-momentum resolved projected density of states of NiO calculated with U values of 0 eV (top), 5 eV (middle), and 10 eV (bottom).

3.2. Polaron distributions at the reduced rutile TiO₂ (110) surface

To further validate our implementation of the “tensorial” DFT+U method in CP2K, we next turn to the description of electron polarons at reduced Rutile TiO₂(110) surfaces. As extensively documented in the specialized literature^{135–137,97}, an accurate description of competing polaron distributions in TiO₂ can be a challenging task beyond the reach of standard local or semi-local XC-functionals and critically dependent on the details of the corrective (e.g., DFT+U) or hybrid DFT approach used. The abundance of available computational results and several energetically competitive polaron configurations at the reduced Rutile TiO₂(110) surface make this system ideal for benchmarking. Based on an established Rutile TiO₂(110) surface model with an oxygen vacancy on the outermost surface layer, we optimized the geometry of several polaron configurations reported in the literature using our implementation of the “tensorial” method in CP2K. We compared the calculated relative energies for such configurations with available experimental and computational results. To be consistent with the computational settings in Ref⁹⁷, we only looked at the results for open-shell singlet polaron structures in this paper. We also investigated the relative stability of triplet-state polaron configurations. The computed results follow an almost identical pattern to those of the open-shell singlet-state case (Table S3 in Ref¹³⁸).

To be consistent with existing studies, we used a (4 × 2) 5-layer slab model as in Refs.¹³⁵ and ⁹⁷.

The bottom two layers were kept in all the geometry optimization processes of a targeted polaron configuration. For consistency with Refs. ¹³⁵ and ⁹⁷, the +U corrections were applied to the Ti *3d* orbitals. To conveniently and efficiently target and optimize a specific final polaron configuration at the end of a geometry optimization process, we utilized the subspace occupancy constraining potential given in Eq. (38) to constrain the electronic structure and accordingly the geometry of the targeted polaron configuration¹³⁸. The potential was gradually reduced to zero before the geometry optimization process ended so that the localized charges and the polarized geometry were not artificially constrained and naturally developed during the optimization process. The U value (3.85 eV for the Ti *3d* subspaces) used in the simulations was calculated using our minimum tracking linear response implementation in CP2K. All force terms contributed by the +U corrective energy given in Eq. (21) were included in the total atomic forces during the geometry optimization process. Further details of our model and computational setup are presented in Ref. ¹³⁸.

Table 1 presents our calculated results for the relative energies of the different polaron configurations studied that are indexed from (a) to (h). A set of plots of their spin density iso-surfaces can be found in Fig. 3 of Ref. ¹³⁸. The relative energy of a given configuration is calculated as the energy difference with the configuration (b) taken as the reference, following what done in Ref. ⁹⁷. As shown in Table 1 (the values in the table were originally reported in Ref. ¹³⁸), the order of the relative energy for the different polaron configurations calculated using our “tensorial” DFT+U implementations in CP2K is exactly the same as the one presented in Ref. ⁹⁷ calculated using DFT+U in FHI-aims. Our results are also consistent with experimental results^{139,140} and other DFT+U or hybrid functional results^{135–137} in that localization of the excess electrons as subsurface polarons [configuration (b)] is energetically favored.

Table 1. Calculated relative energies (eV) for the different polaron configurations studied. The second column presents results in this work, and the third to seventh columns present other computational results in the literature.

configuration index	DFT+U ¹³⁸ (this work)	DFT+U ⁹⁷	DFT+U ¹³⁵	DFT+U ¹³⁶	HSE06 ⁹⁷	HSE06 ¹³⁶
a	-4×10^{-3}	-5×10^{-3}	-	-	-	-
b	0.00	0.00	0.00	0.00	0.00	0.00
c	2×10^{-3}	1×10^{-3}	0.15	-	-	-
d	8×10^{-3}	6×10^{-3}	0.02	-	0.01	-
e	0.25	0.23	0.06	0.28	0.26	0.28
f	0.26	0.40	0.23	0.23	0.45	0.27
g	0.73	0.86	0.63	-	-	-
h	1.08	1.22	0.96	-	-	0.90

3.3. The HOMO-LUMO gap of rutile TiO₂

It has been recently shown that the extension of the DFT+U by inclusion of site-specific Hund’s J corrections (DFT+U+J), in combination with the use of first-principles U and J parameters calculated using the minimum tracking linear-response method, leads to calculated band gaps for

rutile and anatase TiO₂ within the experimental errors. As mentioned in Ref. 26, including the J parameter and using the additional O 2*p* corrections is very beneficial for obtaining the fundamental band gap of rutile and anatase TiO₂ in close agreement with the experimental results. These results provide an ideal reference to further benchmark and validate our implementation of the minimum tracking linear response method for calculating Hubbard U and Hund’s J parameters, which we provide in the following. Following Refs. 61 and 26, the Hund’s J corrective energy contains three parts as given in Eq. 7 in Ref. 61 and Eq. 2 in Ref. 26: a like-spin term, an unlike-spin term, and correction energy specific to the spin channel with minority electronic occupation. In this section, all U and J parameters were calculated from first principles using the minimum tracking linear-response method in the “tensorial” and Löwdin representations implemented in CP2K.

As shown in Ref. 26, in addition to the normal like-spin U correction, the inclusion of like- and unlike-spin J correction terms (II and III in Eq. 2 in Ref. 26) with the exclusion of the J correction for the minority electron spin-channel (IV in Eq. 2 in Ref. 26) does result in a close agreement between simulations and experiments on the material’s fundamental gap. Besides amending the description of exchange effects in open-shell systems, the +J correction is also relevant for correcting the energy and potential of closed-shell systems as approximately described by local or semi-local exchange-correlation functionals²⁷. Following Ref. 26, we consider different E_U functional forms that contain different sets of J-type correction terms. For this set of benchmarks, we used the same geometry (atomic coordinates and cell parameters) as in Ref. 26, specifically a 3×3×5 bulk rutile TiO₂ supercell. The PBE approximation was used as the baseline exchange-correlation functional for the following DFT+U+J calculations. It is worth stressing that for the case of the “tensorial” representation, we stand on the same physical footing as in Ref. 26 regarding projector function selection. In addition, we would like to point out that there is this extra complication of multiple radial projectors per atom in the Löwdin case. The projector functions are the Kohn-Sham DFT solutions to the pseudo-atom problem. Here, we only considered the case of neutral atoms shown in Ref 26 to provide the most accurate band gap of TiO₂. To reduce unnecessary extra coding work to incorporate different sets (I-IV) of corrections and to validate the implementation of the unlike-spin +J correction terms and the subspace constraining potential, here we adopt the reformulation of the (III) and (IV) terms proposed in Ref. 26 for closed-shell systems. The whole (III) terms and the (0, 1/2, 1) (IV) terms are reformulated to a class of like-spin correction terms with a pre-parameter -J and a class of constraining potential terms $\hat{v}_{ext}^{(I)(\sigma)}$ in Eq. (38) with a pre-parameter (J/2, 0, -J/2). The consistency of the explicit DFT+U+J and its reformulation version (like-spin correction + restricted potential) results may be regarded as a mutual verification of the implementations of the explicit DFT+U+J and the constraining potential. All the first-principles linear response U and J parameters for the Ti 3*d* Ti and O 2*p* subspaces are reported in Table S1 in Section 8 of the Supporting Information. A detailed description of the method corresponding to each method serial number and the correction term it contains is provided in Table 2. The calculated band gaps are shown in Table 3.

Table 2. The descriptions of the correction terms included in the simulations. Same method

numbering as in Table 3. The Roman numerals in the parentheses represent the notations of a given correction term in Eq. 2 in Ref. 26. “ ω ” indicates the constraining potentials of Eq. (38) with the given ω value added to the subspaces for both spin channels.

Method No.	Method	Description: the included correction terms
1	DFT+U	only the +U like-spin corrections (I)
2	DFT+U+J (no minority spin term)	the +U like-spin corrections (I) and the +J like- and unlike-spin corrections (II, III)
3	DFT+U _{full} =U-2J, $\omega=J/2$	Same as method No. 2 for non-magnetic systems
4	DFT+U _{full} =U-2J	the +U like-spin corrections (I), the +J like- and unlike-spin corrections (II, III) and the 1/2 of the +J correction terms (0.5×IV) only concerning the spin channel with minor electronic occupation
5	DFT+U _{full} =U-2J, $\omega=-J/2$	the +U like-spin corrections (I), the +J like- and unlike-spin corrections (II, III) and the whole of the +J correction terms (IV) only concerning the spin channel with minor electronic occupation
6	DFT+U _{eff} =U-J	the +U like-spin corrections (I) and the +J like-spin corrections (II)

Table 3. HOMO-LUMO gap (eV) of rutile TiO₂ calculated according to different DFT+U(+J) correction schemes in turn based on various selections of corrected subspaces, treatment of minority spin-terms and the use of “tensorial” or Löwdin subspace representations. “Ti d” indicates the Hubbard corrections were applied only to the Ti 3d subspaces. Conversely, “Ti d, O p” indicates the corrections were applied to both the Ti 3d and O 2p subspaces. Table 2 contains a detailed description of each correction method considered.

Corrected Subspaces	Method No.	“Tensorial” Representation	Löwdin Representation
Ti d	1	2.21	2.50
Ti d, O p	2	3.05	3.17
	3	3.05	3.17
	4	3.21	3.25
	5	3.37	3.33
	6	3.44	3.45
	1	3.69	3.67

As shown in Table 3, applying Hubbard U corrections to the Ti 3d subspace alone cannot fully correct the Kohn-Sham HOMO-LUMO gaps. The calculated band gap values of 2.21 eV and 2.50 eV for the “tensorial” and Löwdin representations remain substantially underestimated with respect to the experimental fundamental gap of 3.03 eV^{141,142}. However, the application of Hubbard U corrections to both the Ti 3d and O 2p subspaces (in both representations) succeeds in opening up the HOMO-LUMO gaps of rutile TiO₂ to values (3.69 eV for the “tensorial” representation and 3.67 eV for the Löwdin representation) which are clearly larger than the experimental fundamental gap 3.03 eV, which is consistent with previous works^{26,27,143}. In the following discussion, we only focus

on the application of U (and J) corrections to both the Ti $3d$ and O $2p$ subspaces. It can be seen in Table 3 that including the like-spin +J corrections by subtracting J from U (the approach is denoted as “DFT+U_{eff}=U-J”) reduces the overestimation of the HOMO-LUMO gaps for both the “tensorial” and Löwdin representations. Specifically, the calculated gaps decrease by 0.25 eV (from 3.69 eV to 3.44 eV) and 0.22 eV (from 3.67 eV to 3.45 eV) in the “tensorial” and Löwdin representation, respectively. After incorporating +J unlike-spin corrections (“DFT+U+J” method No. 2) or “DFT+U_{full}=U-2J, $\omega=J/2$ ” (method No. 3), the calculated band gap is further reduced by 0.39 eV (from 3.44 eV to 3.05 eV) and 0.28 eV (from 3.45 eV to 3.17 eV) for the “tensorial” and Löwdin representations, respectively. Additional inclusion of half of the corrections IV mentioned above (“DFT+U_{full}=U-2J” (method No. 4) increases the calculated HOMO-LUMO gaps. The calculated HOMO-LUMO gap increases by 0.16 eV (from 3.05 eV to 3.21 eV) and 0.08 eV (from 3.17 eV to 3.25 eV) for the “tensorial” and Löwdin representations, respectively. When the whole of the IV terms is included (“DFT+U_{full}=U-2J, $\omega=-J/2$ ” (method No. 5), the calculated HOMO-LUMO gap increases by 0.16 eV (from 3.21 eV to 3.37 eV) and 0.08 eV (from 3.25 eV to 3.33 eV) for the “tensorial” and Löwdin representations, respectively. All of the increases and decreases of the calculated HOMO-LUMO gaps with the specific nature of the correction terms are consistent with the results in Ref. 26. “DFT+U_{full}=U-2J, $\omega=J/2$ ” (method No. 3), which is mathematically identical to “DFT+U+J” (method No. 2) for closed-shell systems should provide the same HOMO-LUMO gap results as those calculated by “DFT+U+J”. Relying on our implementation of the constraining potentials and unlike-spin correction terms in CP2K, the differences of the calculated HOMO-LUMO gaps calculated at “DFT+U_{full}=U-2J, $\omega=J/2$ ” (method No. 3) and “DFT+U+J” (method No. 2) level are systematically smaller than 3.0×10^{-4} eV, for both the “tensorial” and Löwdin representations.

As shown in Table 3, and consistent with the findings in Ref. 26, the functional corrected by the inclusion of the “like”, “unlike”, and “minor” J-type correction terms (method No. 2 (3)) gives the most accurate HOMO-LUMO gap (3.05 eV). This value is only 0.01 eV higher than that calculated using DFT+U+J in ONETEP in conjunction with U and J parameters determined using the minimum tracking linear response method²⁶, and 0.02 eV higher than the experimental fundamental gap of rutile TiO₂^{141,142}. The term IV arises solely due to the double-counting correction in the derivation, which is unlikely to be well described in the underlying exchange-correlation functional and should be ignored²⁶, as also argued in Ref. 61. Our computational results are consistent with the finding in Ref. 26 and support this assertion. For the case of the Löwdin representation, the DFT+U+J predicted HOMO-LUMO gap is 0.14 eV higher than the experimental result. This is not a surprise because the subspaces being corrected in this scheme differ from those in the “tensorial” representation and contain more projector functions. In the current implementation of the DFT+U+J for the Löwdin representation, each Hubbard subspace contains all the existing projector functions localized at a given atomic center with a specific angular momentum quantum number. In addition, the projector functions used for the Löwdin representation undergo a Löwdin orthogonalization with respect to all the basis functions within the simulation cell. This makes the projector function different from the pseudo-atomic solution by mixing contributions from the basis functions on the atom selected for the correction with those from the other atoms.

3.4. Hexahydrated transition metals

In this section, we followed closely the calculations of the first-principles linear-response U and J parameters for the metal $3d$ subspace and the oxygen $2p$ subspace of the hexahydrated transition metal complexes, as presented in Ref. 25, to further validate our implementation of the minimum tracking linear response method. In the hexahydrated transition metal complexes, the $3d$ shells of the transition metal atoms are partially filled (except for the Zn case). Hexahydrated transition metal complexes $[M(H_2O)_6]^{n+}$ are molecular ionic systems (of total charge $+n$) containing a central transition metal ion (M) and six H_2O molecule ligands. Given the octahedral coordination environment, these systems are similar to the elementary units of the corresponding transition metal oxides. Here, a series of hexahydrated transition metals $[M(H_2O)_6]^{2+}$ (M = V, Cr, Mn, Fe, Co, Ni, Cu, Zn) and $[M(H_2O)_6]^{3+}$ (M = Ti, Cr, Mn, Fe, Co) are used for benchmarking the implementation. Depending on the charge states of the metal ion, the tetragonal structure can be in a perfectly symmetric (octahedral) or distorted geometry because of the Jahn-Teller effect^{144–148,25}. Available experimental data indicate that except for low-spin $[Co(H_2O)_6]^{3+}$ and closed-shell $[Zn(H_2O)_6]^{2+}$, all the systems considered have a high-spin ground state^{148–150}. Accordingly, in our simulations, all the electronic configurations of the central ions were set in high spin states, except for $[Co(H_2O)_6]^{3+}$ and $[Zn(H_2O)_6]^{2+}$, which were set in low spin states. We first performed geometry optimization of the hexahydrated transition metal systems with the PBE functional. We then calculated, on the PBE ground states of the PBE optimized geometry, the first-principles linear-response U and J parameters for the central M-ion ($3d$ subspace) and the oxygen atom ($2p$ subspace) closest to the M-ion which was eventually used for all the six oxygen atoms in the complex. For a few cases (e.g., M = V, M = Ti) the procedure was checked to yield $2p$ subspace corrections hardly distinguishable from calculating ligand-specific U and J O $2p$ terms. The projectors for the DFT+U+J subspaces were all obtained by solving the Kohn-Sham DFT problem at the PBE level for the corresponding neutral atom in isolation. Tables S2 and S3 in the Supporting Information report the calculated U and J values, the standard deviation of the corresponding linear fitting, and occupancy numbers within each spin channel of the metal $3d$ and oxygen $2p$ subspaces for the “tensorial” and Löwdin representation.

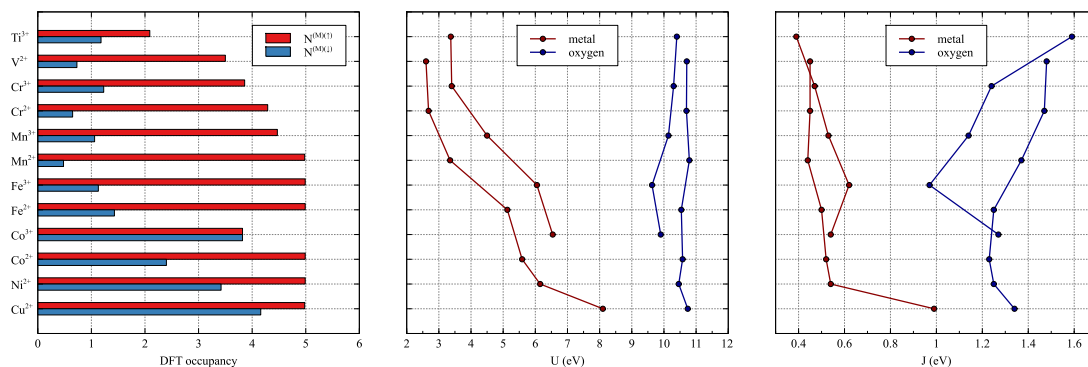


Figure 2. (a)-(c) The plots (the plotting concept was heavily based on Fig. 4 in Ref. 25 in order to visually compare the results of the calculations) of the calculated results in Table S2 for the “tensorial” representation (a) The number of occupancies of the central atom $3d$ subspace where red and blue are used for the α and β spin-channels, respectively. (b) Trend of the U values with the atomic number of the central metal atom. (c) Trend of the J values with the atomic number of the central metal atom. Line segments connect data points from systems with the same total charge. The lines and symbols in panels (b) and (c) are colored red and blue to indicate the results for the metal $3d$ and oxygen $2p$ subspaces, respectively.

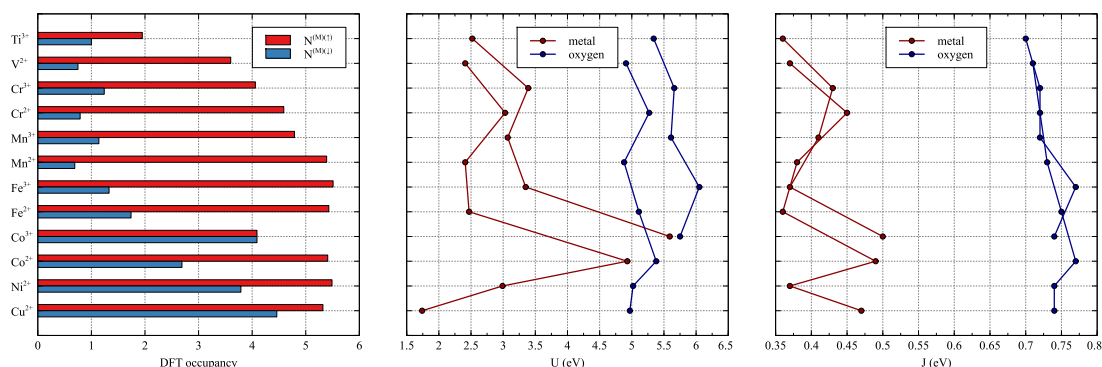


Figure 3. (a)-(c) The plots of the calculated results in Table S3 for the “Löwdin” representation (a) The number of occupancies of the central atom $3d$ subspace where red and blue are used for the α and β spin-channels, respectively. (b) Trend of the U values with the atomic number of the central metal atom. (c) Trend of the J values with the atomic number of the central metal atom. Line segments connect data points from systems with the same total charge. The lines and symbols in panels (b) and (c) are colored red and blue to indicate the results for the metal $3d$ and oxygen $2p$ subspaces, respectively. .

As shown in Table S2 and Fig. 2b, for a given total charge (+2 or +3), the U values of the metal $3d$ subspaces increase with increasing atomic number (except for Zn) in the "tensorial" representation. For a total charge of +2, the U value increases from 2.60 eV (V^{2+}) to 8.10 eV (Cu^{2+}). For a total charge of +3, the U value increases from 3.37 eV (Ti^{3+}) to 6.54 eV (Co^{3+}). Based on our experience, the negative U and J values calculated for the $3d$ subspace of Zn could be related to the basis set used and the projector function defined on this basis. For all the simulations discussed in this section, we used the PBE functional and the recently released MOLOPT basis set (Ti-Ni: TZVP-MOLOPT-PBE-GTH-q12 to TZVP-MOLOPT-PBE-GTH-q18 series; Cu – Zn: TZVP-MOLOPT-PBE-GTH-q11 and TZVP-MOLOPT-PBE-GTH-q12.), which is optimized for molecular systems. The maximum peaks of the radial functions employed in this basis set are generally further away from the center of the atom than in the basis set developed for the modeling of solid systems.

The calculated U values for oxygen $2p$ subspaces do not vary significantly with the atomic number of the metal center. The calculated U values for oxygen $2p$ are all between 9.63 eV and 11.03 eV. Both the trends of gradual increase of the U corrections for the $3d$ metal and relatively stable U

values for oxygen $2p$ with increasing metal atomic number are in agreement with the results shown in Table I-II and Fig. 2(b-c) in Ref. 25. For the same subspace, the values of J that we compute are one order of magnitude smaller than the values of the U corrections. As shown in Table S2 and Fig. 2c, for a given total charge (+2 or +3), the J values of the metal $3d$ subspaces increase with the atomic number of the central metal ion in general. The range of the calculated J values for the $3d$ metal (except for the negative J of Zn) is from 0.39 eV (Ti^{3+}) to 0.99 eV (Cu^{2+}). The calculated J values for oxygen $2p$ are all between 0.97 eV and 1.59 eV. The ratio between calculated U and J corrections for both the $3d$ and $2p$ subspaces, as well as their evolution with the atomic numbers of the central metal ion, are in general agreement with the results shown in Table I-II and Fig. 2(b-c) in Ref. 25.

As shown in Table S3 and Fig. 3(b-c), for the case of the Löwdin representation, no significant dependence of the U or J values on the atomic number of the central metal is observed for either the metal $3d$ or the oxygen $2p$ subspace. In CP2K, the current implementation based on the Löwdin representation adopts an "extended" subspace, which contains all the Löwdin-transformed basis functions centered on a given atom and with the same l character. Combined with the fact that the Löwdin transformation provides less-atomic-orbital-like projector functions, it is not a surprise that the significant dependence of U or J values on the atomic number of the central metal is not there anymore. As in the case of the "tensorial" representation, the calculated J values are generally one order of magnitude smaller than the corresponding U values.

For the "tensorial" representation, the maximum values of the standard deviation of the residuals in the linear regressions for calculating the U and J values for the metal $3d$ and oxygen $2p$ subspaces are 4.7×10^{-4} , 1.1×10^{-4} , 2.7×10^{-4} , and 1.2×10^{-5} eV, respectively. For the Löwdin representation, the maximum values (in the same order as for the "tensorial" representation) are 1.4×10^{-4} , 7.3×10^{-5} , 1.9×10^{-4} , and 1.2×10^{-5} eV, respectively. These values are sufficiently small to be negligible compared with the calculated U and J parameters. This indicates that in our implementations of the minimum tracking linear response method, for all the cases tested in this section, good linearity exists for the dependence of $(V_{Hxc}^{(I)(\uparrow)} + V_{Hxc}^{(I)(\downarrow)})/2$ on $(N^{(I)(\uparrow)} + N^{(I)(\downarrow)})$, and of $-(V_{Hxc}^{(I)(\uparrow)} - V_{Hxc}^{(I)(\downarrow)})/2$ on $(N^{(I)(\uparrow)} - N^{(I)(\downarrow)})$.

The occupation numbers within each spin channel of the metal $3d$ and oxygen $2p$ subspaces presented in Table S2 and Fig. 2(a) are reasonably consistent with those given in Ref. 25. For the case of the Löwdin representation, as shown in Table S3 and Fig. 3(a), the occupation numbers are generally larger than for the "tensorial" representation. Some occupation numbers of the spin α orbital manifolds for the metal $3d$ subspaces exceed "5" which is the expected maximum capacity of a particular spin channel in the $3d$ shell for electrons. This is undesirable but perhaps not surprising because the subspace in the current implementation of the DFT+ U (+ J) and the minimum-tracking linear response method for the Löwdin representation includes all the primarily l -like orbitals centered at the atomic site, as well as effective contributions from all atoms due to the orthonormalization, and thus can accommodate more electrons than the "tensorial" representation

of the nl (e.g., 3d or 2p) subspaces.

3.5. Testing of the DFT+U+J forces

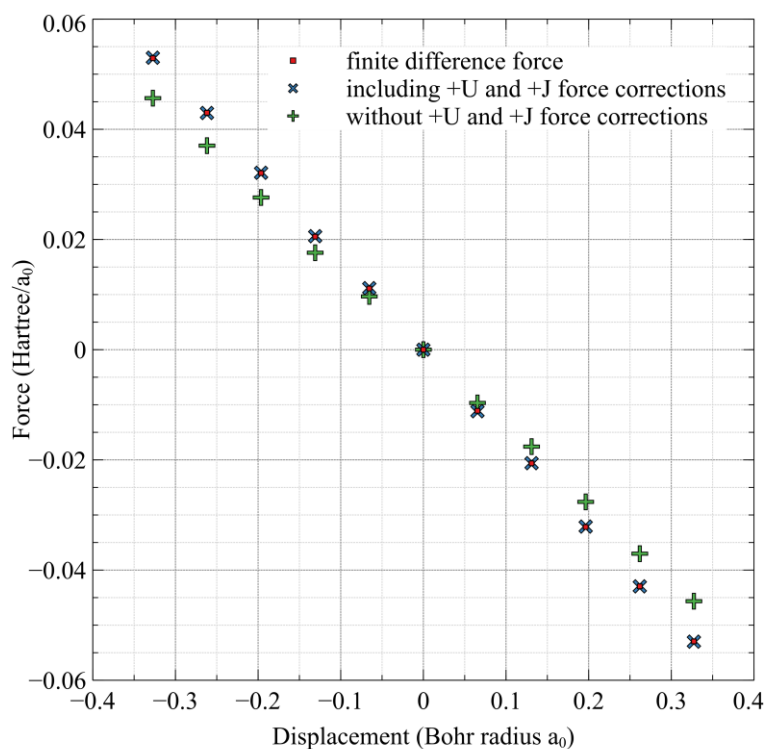
To validate our implementation of the DFT+U+J atomic forces in both the “tensorial” and Löwdin representations, we compared the total analytical forces (including all the DFT+U+J analytical terms) on a selected atom of the simulation cell against with the ones calculated by finite-difference of the changes in total DFT+U+J energies along the corresponding atomic displacements. For comparison, we also present analytical forces without the newly implemented +U and +J force terms by excluding the $\vec{F}_{P,R_k}^{U,J}$ term in Eq. (21) for the “tensorial” representation, and the $\vec{F}_{P,R_k}^{U,J}$ one in Eq. (33) for the Löwdin one.

As in Ref. ⁹³, we adopted NiO, which exhibits an antiferromagnetic ordering of type II (AFII) below a Néel temperature of 523 K, as our test system for the analytical forces contributed by +U and +J corrections. We used a 2×4×4 supercell constructed from the primitive cell reported in Section 11 of the Supporting Information. We adopted symmetry-broken density matrices as the initial guess to obtain an antiferromagnetic ground state. Each Ni atom in a given (111) Ni atomic plane was set with a high-spin atomic occupation by assigning 5 d-electrons to the spin-channel α and 3 d-electrons to the spin-channel β . Each Ni atom in the nearest neighbor Ni atom plane was also set with a high-spin atomic occupation but in antiferromagnetic order by assigning 3 d-electrons to the spin-channel $\alpha(\beta)$ and 5 d-electrons to the spin-channel $\beta(\alpha)$. All O atoms in the simulation cell were set with a closed-shell occupation by assigning 3 electrons each to the α and β spin-channels. +U and +J corrections were applied to all 3d subspaces of the Ni atoms and all the 2p subspaces of the O atoms in the simulation cell. For the U and J parameters in both the “tensorial” and Löwdin representations, we used 5.0 eV and 8.0 eV as U values and 0.5 eV and 0.8 eV as J values on the Ni 3d and O 2p subspaces, respectively. The PBE functional was used as the underlying DFT functional. Pseudopotentials of Goedecker, Teter, and Hutter (GTH) were adopted together with the shorter range molecularly optimized DZVP-MOLOPT-SR-GTH-q18 and DZVP-MOLOPT-SR-GTH-q6 basis sets for Ni and O, respectively. The electron density was represented using an auxiliary plane-wave basis with a 600 Ry density cutoff. In all cases, the k-point sampling was restricted to the Γ -point.

We displaced one Ni atom, initially in a high symmetric position with a (0, 0, 0) fractional position in the supercell, along the forward and reverse direction of the $\vec{r} = (1, 1, 1)$ vector, eventually calculating the total force both analytically (including or neglecting the newly implemented +U and +J force terms) and by finite differences. The displacements along the selected directions range from -0.327 to +0.327 Bohr. For evaluating the forces by finite differences, for every direction of displacement, the Ni atom was displaced forward and backward along $\vec{r} = (1, 1, 1)$ by 1×10^{-6} Bohr.

Figs. 4(a) and 4(b) show the analytical and numerical total atomic forces acting on the Ni atom at

the fractional coordinate (0, 0, 0) across the displacement values for both the “tensorial” and the Löwdin representations. As shown in Figs. 4(a-b), the analytical forces, including the +U and +J terms on the selected Ni atom, agree well with the ones calculated using a finite difference method across the displacement values. However, the analytical forces, not including the +U and +J terms, clearly deviate from the finite difference results calculated from the DFT+U+J total energies. Table 4 reports the ratios (absolute values) of the difference between the analytical force and finite difference force to the finite difference force at a certain displacement of the atom position, where the analytical forces include the contributions of the +U and +J corrective energies. For a displacement with the absolute value between 0.07 Bohr and 0.33 Bohr, the aforementioned ratio does not exceed 1×10^{-3} . At the zero displacement (where the atom is at the equilibrium position), the finite difference force and the difference between the finite difference force and the analytical force are of the same order of magnitude. This results from the fact that the error in the computed finite difference force is of the order of 1×10^{-6} Hartree/Bohr, which is quite significant compared to the analytical force, which is of the order of 1×10^{-8} Hartree/Bohr.



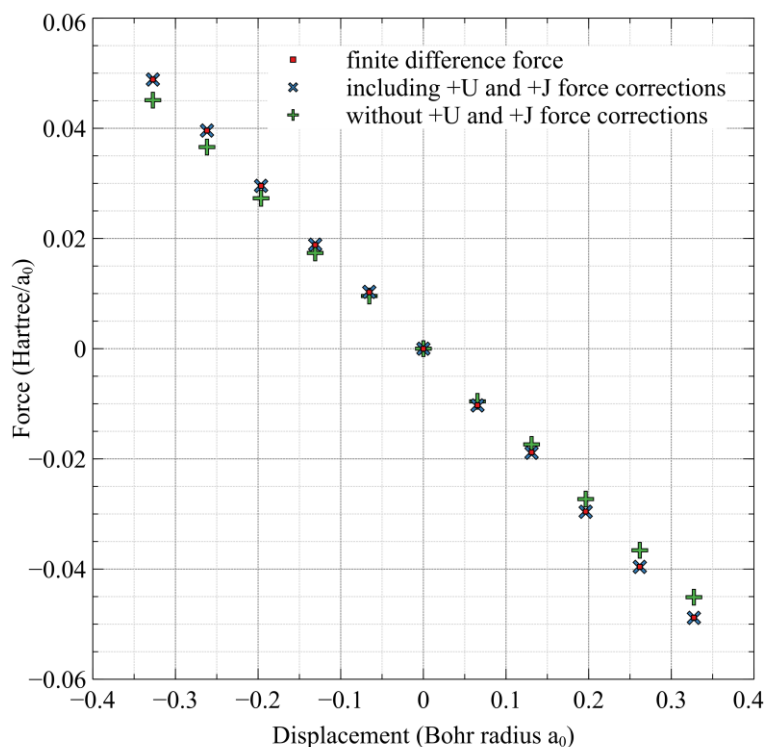


Figure 4. Comparison between the analytical and finite difference total atomic forces acting on the (0, 0, 0) Ni atom for different displacement out of the minimum position for (a) the “tensorial” representation and (b) the Löwdin representation. The squares represent the finite-difference atomic forces. The crosses represent the analytical atomic forces, including the contributions due to the +U and +J energy corrections in CP2K. The plus signs represent the analytical atomic forces, neglecting the contributions due to the +U and +J energy corrections.

Table 4. The absolute values of the ratios of the difference between the analytical force and finite difference force to the finite difference force at a certain displacement of the atom position.

Displacement (a_0)	[Ratio]	
	Tensorial	Löwdin
-0.33	4.1×10^{-5}	1.7×10^{-3}
-0.26	3.2×10^{-4}	9.6×10^{-4}
-0.20	3.1×10^{-4}	1.8×10^{-3}
-0.13	3.1×10^{-3}	4.0×10^{-3}
-0.07	5.8×10^{-3}	5.9×10^{-3}
0.00	9.9×10^{-1}	9.9×10^{-1}
0.07	3.4×10^{-3}	7.3×10^{-3}
0.13	5.1×10^{-3}	1.2×10^{-3}
0.20	1.4×10^{-3}	2.5×10^{-3}
0.26	5.0×10^{-4}	5.8×10^{-5}

0.33	8.9×10^{-4}	8.7×10^{-4}
------	----------------------	----------------------

4. Summary

In this work, we have introduced our implementation in CP2K of the DFT+U+J method based on the "tensorial" representation of subspaces and the +J extension of the existing DFT+U implementation based on the Löwdin representation. In addition to the correction terms for the DFT+U+J energy and potential, we have implemented fully analytical atomic forces due to the DFT+U+J energy. To enable the U and J parameters to be calculated in a first-principles manner as pure ground state quantities, we have additionally implemented in CP2K the recently proposed minimum tracking linear response method. We have benchmarked our additions against recent results in the area to verify all the analytical forms derived and their implementation. Furthermore, we have also tested what Löwdin orthonormalization does to the occupancies, calculated parameters, and derived properties compared to the results for the "tensorial" representation. The DFT+U implementation based on the "tensorial" representation effectively opens up the Kohn-Sham band gap of NiO. It reproduces the relative stability order of electron polarons on the (110) surface of rutile TiO₂. In agreement with previous results,²⁶ we have shown that the present DFT+U+J implementation in combination with self-consistent first-principles U and J parameters and the "tensorial" representation succeeds in calculating a band gap for rutile TiO₂ to within only 0.02 eV from the experimental value. Conversely, the results for the Löwdin representation generally overestimates to the experimental value. In the presented tests on hexahydrated transition metals, and regardless of the specific subspace representation, the linear response J values of a given transition metal *3d* or oxygen *2p* subspace are generally a magnitude smaller than the U parameters, consistent with previous findings in the literature. Good linearities between the subspace potentials after the perturbation (Eq. 38) and the corresponding occupations were generally observed for both subspace representations. For the "tensorial" representation, the calculated trends for the U and J corrections as a function of the atomic number for the central metal and the subspace occupation numbers are consistent with previous results obtained with comparable approaches to the subspace representation. Conversely, due to the artificial extra-site contributions to a given subspace, the subspace occupations in the Löwdin representation are larger than the "tensorial" ones. For some systems, this artifact leads to occupation numbers erroneously exceeding five electrons for a given spin-channel of a *3d* subspace. The calculated U and J parameters in the Löwdin case show a markedly less systematic trend with respect to atomic number than that of the tensorial representation. Our tests on the DFT+U+J analytical forces show them to be in excellent agreement with the numerical ones calculated by finite difference, validating the reliability of our mathematical derivations and implementation in the CP2K code.

Acknowledgements

This work was financially supported by the National Key Research and Development Program of China (No. 2022YFB4200501). The work was supported by the National Natural Science

Foundation of China (52225308). Z. C. is grateful to Beijing Computational Science Research Center for their support and facilities, which enabled the successful completion of this work during Z. C.'s doctoral tenure. L.M. L. and G. T. acknowledge support by the Royal Society Newton Advanced Fellowship scheme (grant No. NAF\R1\180242). D.O'R. acknowledges the support of a research grant from Science Foundation Ireland (SFI), co-funded under the European Regional Development Fund under Prime Award No. 12/RC/2278 and 12/RC/2278_P2.

Supporting Information

1. The full derivations of the DFT+U+J potential matrix given in Eq. (20)

$$\begin{aligned}
(H^{U,J})_{\beta\gamma}^{\sigma} &= \frac{\partial E_{U,J}}{\partial D^{(\sigma)\gamma\beta}} \\
&= \sum_{I\sigma'} \left\{ \frac{U^{(I)} - J^{(I)}}{2} \cdot \frac{\partial \left[P_{i\theta}^{(I)} D^{(\sigma')\theta i} - P_{\zeta\eta}^{(I)} D^{(\sigma')\eta\mu} P_{\mu\nu}^{(I)} D^{(\sigma')\nu\zeta} \right]}{\partial D^{(\sigma)\gamma\beta}} + \frac{J^{(I)}}{2} \right. \\
&\quad \left. \cdot \frac{\partial \left[P_{\varepsilon\kappa}^{(I)} D^{(\sigma')\kappa\sigma} P_{\sigma\pi}^{(I)} D^{(-\sigma')\pi\varepsilon} \right]}{\partial D^{(\sigma)\gamma\beta}} \right\} \\
&= \sum_I \left\{ \frac{U^{(I)} - J^{(I)}}{2} \cdot \frac{\partial \left[P_{i\theta}^{(I)} D^{(\sigma)\theta i} - P_{\zeta\eta}^{(I)} D^{(\sigma)\eta\mu} P_{\mu\nu}^{(I)} D^{(\sigma)\nu\zeta} \right]}{\partial D^{(\sigma)\gamma\beta}} + \frac{J^{(I)}}{2} \right. \\
&\quad \left. \cdot \frac{\partial \left[P_{\varepsilon\kappa}^{(I)} D^{(\sigma)\kappa\sigma} P_{\sigma\pi}^{(I)} D^{(-\sigma)\pi\varepsilon} + P_{\varepsilon'\kappa'}^{(I)} D^{(-\sigma)\kappa'o'} P_{\sigma'\pi'}^{(I)} D^{(\sigma)\pi'\varepsilon'} \right]}{\partial D^{(\sigma)\gamma\beta}} \right\} \\
&= \sum_I \left\{ \frac{U^{(I)} - J^{(I)}}{2} \cdot \left[P_{i\theta}^{(I)} \delta_{\gamma}^{\theta} \delta_{\beta}^i - P_{\zeta\eta}^{(I)} \delta_{\gamma}^{\eta} \delta_{\beta}^{\mu} P_{\mu\nu}^{(I)} D^{(\sigma)\nu\zeta} - P_{\zeta\eta}^{(I)} D^{(\sigma)\eta\mu} P_{\mu\nu}^{(I)} \delta_{\gamma}^{\nu} \delta_{\beta}^{\zeta} \right] + \frac{J^{(I)}}{2} \right. \\
&\quad \left. \cdot \left[P_{\varepsilon\kappa}^{(I)} \delta_{\gamma}^{\kappa} \delta_{\beta}^{\sigma} P_{\sigma\pi}^{(I)} D^{(-\sigma)\pi\varepsilon} + P_{\varepsilon'\kappa'}^{(I)} D^{(-\sigma)\kappa'o'} P_{\sigma'\pi'}^{(I)} \delta_{\gamma}^{\pi'} \delta_{\beta}^{\varepsilon'} \right] \right\} \\
&= \sum_I \left\{ \frac{U^{(I)} - J^{(I)}}{2} \cdot \left[P_{\beta\gamma}^{(I)} - 2P_{\beta\nu}^{(I)} D^{(\sigma)\nu\zeta} P_{\zeta\gamma}^{(I)} \right] + \frac{J^{(I)}}{2} \cdot \left[2P_{\beta\pi}^{(I)} D^{(-\sigma)\pi\varepsilon} P_{\varepsilon\gamma}^{(I)} \right] \right\} \\
&= \sum_I V_{\beta b}^{(I)} \left\{ \frac{U^{(I)} - J^{(I)}}{2} \cdot \left[O^{(I)bc} - 2 \cdot O^{(I)bd} W_{dk}^{(I)} D^{(\sigma)\kappa i} V_{if}^{(I)} O^{(I)fc} \right] + \frac{J^{(I)}}{2} \right. \\
&\quad \left. \cdot \left[2 \cdot O^{(I)bg} W_{g\theta}^{(I)} D^{(-\sigma)\theta\nu} V_{vi}^{(I)} O^{(I)ic} \right] \right\} W_{c\gamma}^{(I)} \\
&= \sum_I V_{\beta b}^{(I)} \left\{ \frac{U^{(I)} - J^{(I)}}{2} \cdot \left[O^{(I)bc} - 2 \cdot O^{(I)bd} n_d^{(I)(\sigma)c} \right] + \frac{J^{(I)}}{2} \cdot \left[2 \cdot O^{(I)bg} n_g^{(I)(-\sigma)c} \right] \right\} W_{c\gamma}^{(I)} \\
&= \sum_I V_{\beta b}^{(I)} O^{(I)bd} \left\{ \frac{U^{(I)} - J^{(I)}}{2} \cdot \left[\delta_d^c - 2 \cdot n_d^{(I)(\sigma)c} \right] + J^{(I)} n_d^{(I)(-\sigma)c} \right\} W_{c\gamma}^{(I)}
\end{aligned}$$

$$= \sum_I S_{\beta,(I)b\alpha'} a^{(I)\alpha'} O^{(I)bd} \left\{ \frac{U^{(I)} - J^{(I)}}{2} \cdot [\delta_d^c - 2 \cdot n_d^{(I)(\sigma)c}] + J^{(I)} n_d^{(I)(-\sigma)c} \right\} a^{(I)\alpha*} S_{(I)c\alpha,\gamma}.$$

2. The full derivations of the $\frac{\partial E_{U,J}}{\partial P_{\beta\gamma}^{(I')}}$ matrix given in Eq. (22)

$$\begin{aligned} & \frac{\partial E_{U,J}}{\partial P_{\beta\gamma}^{(I')}} \\ &= \frac{\partial \left[\frac{1}{2} \sum_{I\sigma} (U^{(I)} - J^{(I)}) (P_{\varepsilon\kappa}^{(I)} D^{(\sigma)\kappa\varepsilon} - P_{\nu\theta}^{(I)} D^{(\sigma)\theta\varepsilon} P_{\varepsilon l}^{(I)} D^{(\sigma)l\nu}) + \frac{1}{2} \sum_{I\sigma} J^{(I)} P_{o\mu}^{(I)} D^{(\sigma)\mu\pi} P_{\pi\rho}^{(I)} D^{(-\sigma)\rho o} \right]}{\partial P_{\beta\gamma}^{(I')}} \\ &= \frac{1}{2} \sum_{\sigma} \left[(U^{(I')} - J^{(I')}) \left(\frac{\partial (P_{\varepsilon\kappa}^{(I')} D^{(\sigma)\kappa\varepsilon})}{\partial P_{\beta\gamma}^{(I')}} - \frac{\partial (P_{\nu\theta}^{(I')} D^{(\sigma)\theta\varepsilon} P_{\varepsilon l}^{(I')} D^{(\sigma)l\nu})}{\partial P_{\beta\gamma}^{(I')}} \right) \right. \\ & \quad \left. + J^{(I')} \frac{\partial (P_{o\mu}^{(I')} D^{(\sigma)\mu\pi} P_{\pi\rho}^{(I')} D^{(-\sigma)\rho o})}{\partial P_{\beta\gamma}^{(I')}} \right] \\ &= \frac{1}{2} \sum_{\sigma} \left[(U^{(I')} - J^{(I')}) (\delta_{\varepsilon}^{\beta} \delta_{\kappa}^{\gamma} D^{(\sigma)\kappa\varepsilon} - \delta_{\nu}^{\beta} \delta_{\theta}^{\gamma} D^{(\sigma)\theta\varepsilon} P_{\varepsilon l}^{(I')} D^{(\sigma)l\nu} - P_{\nu\theta}^{(I')} D^{(\sigma)\theta\varepsilon} \delta_{\varepsilon}^{\beta} \delta_l^{\gamma} D^{(\sigma)l\nu}) \right. \\ & \quad \left. + J^{(I')} (\delta_o^{\beta} \delta_{\mu}^{\gamma} D^{(\sigma)\mu\pi} P_{\pi\rho}^{(I')} D^{(-\sigma)\rho o} + P_{o\mu}^{(I')} D^{(\sigma)\mu\pi} \delta_{\pi}^{\beta} \delta_{\rho}^{\gamma} D^{(-\sigma)\rho o}) \right] \\ &= \frac{1}{2} \sum_{\sigma} \left[(U^{(I')} - J^{(I')}) (D^{(\sigma)\gamma\beta} - D^{(\sigma)\gamma\varepsilon} P_{\varepsilon l}^{(I')} D^{(\sigma)l\beta} - D^{(\sigma)\gamma\nu} P_{\nu\theta}^{(I')} D^{(\sigma)\theta\beta}) \right. \\ & \quad \left. + J^{(I')} (D^{(\sigma)\gamma\pi} P_{\pi\rho}^{(I')} D^{(-\sigma)\rho\beta} + D^{(-\sigma)\gamma o} P_{o\mu}^{(I')} D^{(\sigma)\mu\beta}) \right] \\ &= \frac{1}{2} \sum_{\sigma} \left[(U^{(I')} - J^{(I')}) (D^{(\sigma)\gamma\beta} - 2 \cdot D^{(\sigma)\gamma\varepsilon} P_{\varepsilon l}^{(I')} D^{(\sigma)l\beta}) + J^{(I')} (2 \cdot D^{(\sigma)\gamma\pi} P_{\pi\rho}^{(I')} D^{(-\sigma)\rho\beta}) \right]. \end{aligned}$$

3. The full derivations of the $\frac{\partial E_{U,J}}{\partial P_{\beta\gamma}^{(I')}}$ matrix given in Eq. (24)

$$\begin{aligned} \frac{\partial P_{\beta\gamma}^{(I')}}{\partial R_k^{a_i}} &= \frac{\partial (\langle \phi_{\beta} | \phi_{m'\alpha'}^{(I')} \rangle)}{\partial R_k^{a_i}} a^{(I')\alpha'} O^{(I')m'm} W_{m\gamma}^{(I')} + V_{\beta m'}^{(I')} O^{(I')m'm} a^{(I')\alpha*} \frac{\partial (\langle \phi_{m\alpha}^{(I')} | \phi_{\gamma} \rangle)}{\partial R_k^{a_i}} \\ &= \frac{\langle \partial \phi_{\beta} | \phi_{m'\alpha'}^{(I')} \rangle + \langle \phi_{\beta} | \partial \phi_{m'\alpha'}^{(I')} \rangle}{\partial R_k^{a_i}} a^{(I')\alpha'} O^{(I')m'm} W_{m\gamma}^{(I')} \\ & \quad + V_{\beta m'}^{(I')} O^{(I')m'm} a^{(I')\alpha*} \frac{\langle \partial \phi_{m\alpha}^{(I')} | \phi_{\gamma} \rangle + \langle \phi_{m\alpha}^{(I')} | \partial \phi_{\gamma} \rangle}{\partial R_k^{a_i}} \\ &= \left[(\delta_{a_i \phi_{\beta}} G_{\beta,(I')m'\alpha'}^k - G_{\beta,(I')m'\alpha'}^k \delta_{a_i, \phi_{\beta}}) a^{(I')\alpha'} \right] O^{(I')m'm} W_{m\gamma}^{(I')} \\ & \quad + V_{\beta m'}^{(I')} O^{(I')m'm} \left[a^{(I')\alpha*} (\delta_{a_i, \phi_{\gamma}} G_{(I')m\alpha,\gamma}^k - G_{(I')m\alpha,\gamma}^k \delta_{a_i, \phi_{\gamma}}) \right] \end{aligned}$$

$$\begin{aligned}
&= L_{\beta,(I')m'}^{k,I} O^{(I')m'm} W_{m\gamma}^{(I')} + V_{\beta m'}^{(I')} O^{(I')m'm} \left(L_{(I')m,\gamma}^{k,I} \right)^* \\
&= \left[\left(L^{k,I} O^{(I')} W^{(I')} \right) + \left(L^{k,I} O^{(I')} W^{(I')} \right)^\dagger \right]_{\beta\gamma}.
\end{aligned}$$

4. The full derivations of the occupation matrix in the Löwdin representation given in Eq. (30)

$$\begin{aligned}
\bar{n}_{m\alpha}^{(I)(\sigma)m'\alpha'} &= \langle \bar{\phi}_{(I)m\alpha} | \hat{\rho}^{(\sigma)} | \bar{\phi}_{(I)m'\alpha'} \rangle \\
&= (A^{-1})_{(I)m\alpha,\gamma} \langle \phi_\gamma | \psi_i^{(\sigma)} \rangle f_i^{(\sigma)} \langle \psi_i^{(\sigma)} | \phi_{\gamma'} \rangle (A^{-1})_{\gamma',(I)m'\alpha'} \\
&= (A^{-1})_{(I)m\alpha,\gamma} S_{\gamma\zeta} \langle \phi_\zeta | \psi_i^{(\sigma)} \rangle f_i^{(\sigma)} \langle \psi_i^{(\sigma)} | \phi_{\zeta'} \rangle S_{\zeta'\gamma'} (A^{-1})_{\gamma',(I)m'\alpha'} \\
&= (A^{-1})_{(I)m\alpha,\gamma} S_{\gamma\zeta} D^{(\sigma)\zeta,\zeta'} S_{\zeta'\gamma'} (A^{-1})_{\gamma',(I)m'\alpha'} \\
&= (AD^{(\sigma)}A)_{(I)m\alpha,(I)m'\alpha'}.
\end{aligned}$$

The full derivations of the +J potential matrix in the Löwdin representation given in Eq. (32)

$$\begin{aligned}
(H^J)_{\beta\gamma}^\sigma &= \frac{\partial E_J}{\partial D^{(\sigma)\beta\gamma}} \\
&= \frac{\partial \frac{1}{2} \sum_{I\sigma} J^{(I)} (AD^{(\sigma)}A)_{(I)m'''\alpha''',(I)m'''\alpha''',(I)m'''\alpha''',(AD^{(-\sigma)}A)_{(I)m'''\alpha''',(I)m'''\alpha'''}}{\partial D^{(\sigma)\beta\gamma}} \\
&= \frac{\partial \frac{1}{2} \sum_{I\sigma} J^{(I)} A_{(I)m\alpha,\mu} (D^{(\sigma)})^{\mu\nu} A_{\nu,(I)m'\alpha'} A_{(I)m'\alpha',o} (D^{(-\sigma)})^{o\ell} A_{\ell,(I)m\alpha}}{\partial D^{(\sigma)\beta\gamma}} \\
&= \frac{1}{2} \sum_I J^{(I)} A_{(I)m\alpha,\mu} \delta_\beta^\mu \delta_\gamma^\nu A_{\nu,(I)m'\alpha'} A_{(I)m'\alpha',o} (D^{(-\sigma)})^{o\ell} A_{\ell,(I)m\alpha} \\
&\quad + J^{(I)} A_{(I)m''\alpha'',\mu'} (D^{(-\sigma)})^{\mu'\nu'} A_{\nu',(I)m'''\alpha'''} A_{(I)m'''\alpha''',o'} \delta_\beta^{o'} \delta_\gamma^{\ell'} A_{\ell',(I)m''\alpha''} \\
&= \frac{1}{2} \sum_I J^{(I)} A_{(I)m\alpha,\beta} A_{\gamma,(I)m'\alpha'} A_{(I)m'\alpha',o} (D^{(-\sigma)})^{o\ell} A_{\ell,(I)m\alpha} \\
&\quad + J^{(I)} A_{(I)m''\alpha'',\mu'} (D^{(-\sigma)})^{\mu'\nu'} A_{\nu',(I)m'''\alpha'''} A_{(I)m'''\alpha''',\beta} A_{\gamma,(I)m''\alpha''} \\
&= \frac{1}{2} \sum_I J^{(I)} A_{\gamma,(I)m'\alpha'} A_{(I)m'\alpha',o} (D^{(-\sigma)})^{o\ell} A_{\ell,(I)m\alpha} A_{(I)m\alpha,\beta} \\
&\quad + J^{(I)} A_{\gamma,(I)m''\alpha''} A_{(I)m''\alpha'',\mu'} (D^{(-\sigma)})^{\mu'\nu'} A_{\nu',(I)m'''\alpha'''} A_{(I)m'''\alpha''',\beta} \\
&= \frac{1}{2} \sum_I J^{(I)} A_{\gamma,(I)m'\alpha'} (AD^{(-\sigma)}A)_{(I)m'\alpha',(I)m\alpha} A_{(I)m\alpha,\beta} \\
&\quad + J^{(I)} A_{\gamma,(I)m''\alpha''} (AD^{(-\sigma)}A)_{(I)m''\alpha'',(I)m'''\alpha'''} A_{(I)m'''\alpha''',\beta}.
\end{aligned}$$

5. The full derivations of $\frac{\partial E_{UJ}}{\partial A_{\beta\gamma}}$ in the Löwdin representation given in Eq. (34)

$$\begin{aligned}
\frac{\partial E_{U,J}}{\partial A_{\beta\gamma}} &= \frac{\partial \left[\frac{1}{2} \sum_{I\sigma} (U^{(I)} - J^{(I)}) \left(\begin{array}{c} A_{(I)m\alpha,\mu} (D^{(\sigma)})^{\mu\nu} A_{\nu,(I)m\alpha} \\ -A_{(I)m'\alpha',o} (D^{(\sigma)})^{ol} A_{l,(I)m''\alpha''} A_{(I)m''\alpha'',\theta} (D^{(\sigma)})^{\theta\kappa} A_{\kappa,(I)m'\alpha'} \end{array} \right) \right. \\
&\quad \left. + \frac{1}{2} \sum_{I\sigma} J^{(I)} A_{(I)m'''\alpha''',\varepsilon} (D^{(\sigma)})^{\varepsilon\zeta} A_{\zeta,(I)m''''\alpha''''} A_{(I)m''''\alpha'''',\pi} (D^{(-\sigma)})^{\pi\eta} A_{\eta,(I)m'''\alpha'''} \right]}{\partial A_{\beta\gamma}} \\
&= \frac{1}{2} \sum_{I\sigma} (U^{(I)} - J^{(I)}) \left(\begin{array}{c} \delta_{gl((I)m\alpha)}^{\beta} \delta_{\mu}^{\gamma} (D^{(\sigma)})^{\mu\nu} A_{\nu,(I)m\alpha} + A_{(I)m\alpha,\mu} (D^{(\sigma)})^{\mu\nu} \delta_{\nu}^{\beta} \delta_{gl((I)m\alpha)}^{\gamma} \\ -\delta_{gl((I)m'\alpha')}^{\beta} \delta_o^{\gamma} (D^{(\sigma)})^{ol} A_{l,(I)m''\alpha''} A_{(I)m''\alpha'',\theta} (D^{(\sigma)})^{\theta\kappa} A_{\kappa,(I)m'\alpha'} \\ -A_{(I)m'\alpha',o} (D^{(\sigma)})^{ol} \delta_l^{\beta} \delta_{gl((I)m''\alpha'')}^{\gamma} A_{(I)m''\alpha'',\theta} (D^{(\sigma)})^{\theta\kappa} A_{\kappa,(I)m'\alpha'} \\ -A_{(I)m'\alpha',o} (D^{(\sigma)})^{ol} A_{l,(I)m''\alpha''} \delta_{gl((I)m''\alpha'')}^{\beta} \delta_{\theta}^{\gamma} (D^{(\sigma)})^{\theta\kappa} A_{\kappa,(I)m'\alpha'} \\ -A_{(I)m'\alpha',o} (D^{(\sigma)})^{ol} A_{l,(I)m''\alpha''} A_{(I)m''\alpha'',\theta} (D^{(\sigma)})^{\theta\kappa} \delta_{\kappa}^{\beta} \delta_{gl((I)m'\alpha')}^{\gamma} \end{array} \right) \\
&+ \frac{1}{2} \sum_{I\sigma} J^{(I)} \left(\begin{array}{c} \delta_{gl((I)m'''\alpha''')}^{\beta} \delta_{\varepsilon}^{\gamma} (D^{(\sigma)})^{\varepsilon\zeta} A_{\zeta,(I)m''''\alpha''''} A_{(I)m''''\alpha'''',\pi} (D^{(-\sigma)})^{\pi\eta} A_{\eta,(I)m'''\alpha'''} \\ +A_{(I)m'''\alpha''',\varepsilon} (D^{(\sigma)})^{\varepsilon\zeta} \delta_{\zeta}^{\beta} \delta_{gl((I)m''''\alpha'''')}^{\gamma} A_{(I)m''''\alpha'''',\pi} (D^{(-\sigma)})^{\pi\eta} A_{\eta,(I)m'''\alpha'''} \\ +A_{(I)m'''\alpha''',\varepsilon} (D^{(\sigma)})^{\varepsilon\zeta} A_{\zeta,(I)m''''\alpha''''} \delta_{gl((I)m''''\alpha'''')}^{\beta} \delta_{\pi}^{\gamma} (D^{(-\sigma)})^{\pi\eta} A_{\eta,(I)m'''\alpha'''} \\ +A_{(I)m'''\alpha''',\varepsilon} (D^{(\sigma)})^{\varepsilon\zeta} A_{\zeta,(I)m''''\alpha''''} A_{(I)m''''\alpha'''',\pi} (D^{(-\sigma)})^{\pi\eta} \delta_{\eta}^{\beta} \delta_{gl((I)m'''\alpha''')}^{\gamma} \end{array} \right) \\
&= \frac{1}{2} \sum_{I\sigma} (U^{(I)} - J^{(I)}) \left(\begin{array}{c} (D^{(\sigma)})^{\gamma\nu} A_{\nu,(I)m\alpha} \delta_{\beta}^{gl((I)m\alpha)} + \delta_{gl((I)m\alpha)}^{\gamma} A_{(I)m\alpha,\mu} (D^{(\sigma)})^{\mu\beta} \\ -(D^{(\sigma)})^{\gamma l} A_{l,(I)m''\alpha''} A_{(I)m''\alpha'',\theta} (D^{(\sigma)})^{\theta\kappa} A_{\kappa,(I)m'\alpha'} \delta_{gl((I)m'\alpha')}^{\beta} \\ -\delta_{gl((I)m''\alpha'')}^{\gamma} A_{(I)m''\alpha'',\theta} (D^{(\sigma)})^{\theta\kappa} A_{\kappa,(I)m'\alpha'} A_{(I)m'\alpha',o} (D^{(\sigma)})^{o\beta} \\ -(D^{(\sigma)})^{\gamma\kappa} A_{\kappa,(I)m'\alpha'} A_{(I)m'\alpha',o} (D^{(\sigma)})^{ol} A_{l,(I)m''\alpha''} \delta_{gl((I)m''\alpha'')}^{\beta} \\ -\delta_{gl((I)m'\alpha')}^{\gamma} A_{(I)m'\alpha',o} (D^{(\sigma)})^{ol} A_{l,(I)m''\alpha''} A_{(I)m''\alpha'',\theta} (D^{(\sigma)})^{\theta\beta} \end{array} \right) \\
&+ \frac{1}{2} \sum_{I\sigma} J^{(I)} \left(\begin{array}{c} (D^{(\sigma)})^{\gamma\zeta} A_{\zeta,(I)m''''\alpha''''} A_{(I)m''''\alpha'''',\pi} (D^{(-\sigma)})^{\pi\eta} A_{\eta,(I)m'''\alpha'''} \delta_{gl((I)m'''\alpha''')}^{\beta} \\ +\delta_{gl((I)m''''\alpha'''')}^{\gamma} A_{(I)m''''\alpha'''',\pi} (D^{(-\sigma)})^{\pi\eta} A_{\eta,(I)m'''\alpha'''} A_{(I)m'''\alpha''',\varepsilon} (D^{(\sigma)})^{\varepsilon\beta} \\ +(D^{(-\sigma)})^{\gamma\eta} A_{\eta,(I)m'''\alpha'''} A_{(I)m'''\alpha''',\varepsilon} (D^{(\sigma)})^{\varepsilon\zeta} A_{\zeta,(I)m''''\alpha''''} \delta_{gl((I)m''''\alpha'''')}^{\beta} \\ +\delta_{gl((I)m'''\alpha''')}^{\gamma} A_{(I)m'''\alpha''',\varepsilon} (D^{(\sigma)})^{\varepsilon\zeta} A_{\zeta,(I)m''''\alpha''''} A_{(I)m''''\alpha'''',\pi} (D^{(-\sigma)})^{\pi\beta} \end{array} \right) .
\end{aligned}$$

Define K as

$$K_{(I)m\alpha}^{(\sigma)\gamma} = (D^{(\sigma)})^{\gamma\mu} A_{\mu,(I)m\alpha}.$$

Then it gives

$$\begin{aligned}
\frac{\partial E_{U,J}}{\partial A_{\beta\gamma}} = & \frac{1}{2} \sum_{I\sigma} (U^{(I)} - J^{(I)}) \left(\begin{array}{l} K_{(I)m\alpha}^{(\sigma)\gamma} \delta_{\beta}^{gl(I)m\alpha} + \delta_{\gamma}^{gl(I)m\alpha} \left((K^{(\sigma)})^T \right)_{(I)m\alpha}^{\beta} \\ - K_{(I)m''\alpha''}^{(\sigma)\gamma} A_{(I)m''\alpha'',\eta} K_{(I)m'\alpha'}^{(\sigma)\eta} \delta_{\beta}^{gl(I)m'\alpha'} \\ - \delta_{\gamma}^{gl(I)m''\alpha''} \left((K^{(\sigma)})^T \right)_{(I)m''\alpha''}^{\mu} A_{\mu,(I)m'\alpha'} \left((K^{(\sigma)})^T \right)_{(I)m'\alpha'}^{\beta} \\ - K_{(I)m'\alpha'}^{(\sigma)\gamma} A_{(I)m'\alpha',\kappa} K_{(I)m''\alpha''}^{(\sigma)\kappa} \delta_{\beta}^{gl(I)m''\alpha''} \\ - \delta_{\gamma}^{gl(I)m'\alpha'} \left((K^{(\sigma)})^T \right)_{(I)m'\alpha'}^{\pi} A_{\pi,(I)m''\alpha''} \left((K^{(\sigma)})^T \right)_{(I)m''\alpha''}^{\beta} \end{array} \right) \\
& + \frac{1}{2} \sum_{I\sigma} J^{(I)} \left(\begin{array}{l} K_{(I)m''''\alpha''''}^{(\sigma)\gamma} A_{(I)m''''\alpha'''',\theta} K_{(I)m''''\alpha''''}^{(-\sigma)\theta} \delta_{\beta}^{gl(I)m''''\alpha''''} \\ + \delta_{\gamma}^{gl(I)m''''\alpha''''} \left((K^{(\sigma)})^T \right)_{(I)m''''\alpha''''}^o A_{o,(I)m''''\alpha''''} \left((K^{(-\sigma)})^T \right)_{(I)m''''\alpha''''}^{\beta} \\ + K_{(I)m''''\alpha''''}^{(\sigma)\gamma} A_{(I)m''''\alpha'''',\iota} K_{(I)m''''\alpha''''}^{(-\sigma)\iota} \delta_{\beta}^{gl(I)m''''\alpha''''} \\ + \delta_{\gamma}^{gl(I)m''''\alpha''''} \left((K^{(-\sigma)})^T \right)_{(I)m''''\alpha''''}^{\rho} A_{\rho,(I)m''''\alpha''''} \left((K^{(\sigma)})^T \right)_{(I)m''''\alpha''''}^{\beta} \end{array} \right) \\
= & \frac{1}{2} \sum_{I\sigma} (U^{(I)} - J^{(I)}) \left(\begin{array}{l} \left(K_{(I)m\alpha}^{(\sigma)\gamma} - 2 \cdot K_{(I)m'\alpha'}^{(\sigma)\gamma} A_{(I)m'\alpha',\mu} K_{(I)m\alpha}^{(\sigma)\mu} \right) \delta_{\beta}^{gl(I)m\alpha} \\ + \delta_{\gamma}^{gl(I)m\alpha} \left(\left((K^{(\sigma)})^T \right)_{(I)m\alpha}^{\beta} - 2 \cdot \left((K^{(\sigma)})^T \right)_{(I)m\alpha}^{\nu} A_{\nu,(I)m'\alpha'} \left((K^{(\sigma)})^T \right)_{(I)m'\alpha'}^{\beta} \right) \end{array} \right) \\
& + \frac{1}{2} \sum_{I\sigma} J^{(I)} \left(\begin{array}{l} 2 \cdot K_{(I)m''''\alpha''''}^{(\sigma)\gamma} A_{(I)m''''\alpha'''',\iota} K_{(I)m''''\alpha''''}^{(-\sigma)\iota} \delta_{\beta}^{gl(I)m''''\alpha''''} \\ + 2 \cdot \delta_{\gamma}^{gl(I)m''''\alpha''''} \left((K^{(\sigma)})^T \right)_{(I)m''''\alpha''''}^o A_{o,(I)m''''\alpha''''} \left((K^{(-\sigma)})^T \right)_{(I)m''''\alpha''''}^{\beta} \end{array} \right).
\end{aligned}$$

6. The full derivations of $V_{Hxc}^{(I)(\sigma)}$ in the ‘‘tensorial’’ representation given in Eq. (45)

$$\begin{aligned}
V_{Hxc}^{(I)(\sigma)} & \equiv \frac{Tr \left[\hat{V}_{Hxc}^{(\sigma)} \hat{P}^{(I)} \right]}{Tr \left[\hat{P}^{(I)} \right]} \\
& = \frac{\sum_r \langle \phi_{(r)} | \hat{V}_{Hxc}^{(\sigma)} | \varphi^{(I)m} \rangle \langle \varphi_m^{(I)} | \phi_{(r)} \rangle}{\sum_{r'} \langle \phi_{(r')} | \varphi^{(I)m''} \rangle \langle \varphi_{m''}^{(I)} | \phi_{(r')} \rangle} \\
& = \frac{\sum_r \langle \phi_{(r)} | \hat{V}_{Hxc}^{(\sigma)} | \varphi_{m'}^{(I)} \rangle O^{(I)m'm} \langle \varphi_m^{(I)} | \phi_{(r)} \rangle}{\sum_{r'} \langle \phi_{(r')} | \varphi_{m''''}^{(I)} \rangle O^{(I)m''''m''} \langle \varphi_{m''}^{(I)} | \phi_{(r')} \rangle} \\
& = \frac{\sum_r \langle \phi_{(r)} | \hat{V}_{Hxc}^{(\sigma)} | \phi_{m'\alpha'}^{(I)} \rangle a^{(I)\alpha'} O^{(I)m'm} a^{(I)\alpha*} \langle \phi_{m\alpha}^{(I)} | \phi_{(r)} \rangle}{\sum_{r'} \langle \phi_{(r')} | \phi_{m''''\alpha''''}^{(I)} \rangle a^{(I)\alpha''''} O^{(I)m''''m''} a^{(I)\alpha''*} \langle \phi_{m''\alpha''}^{(I)} | \phi_{(r')} \rangle} \\
& = \frac{\sum_r \left(V_{Hxc}^{(\sigma)} \right)_{(r),(I)m'\alpha'} a^{(I)\alpha'} O^{(I)m'm} a^{(I)\alpha*} \delta_{gl(I)m\alpha}^{(r)}}{\sum_{r'} S_{(r'),(I)m''''\alpha''''} a^{(I)\alpha''''} O^{(I)m''''m''} a^{(I)\alpha''*} \delta_{gl(I)m''\alpha''}^{(r')}} \\
& = \frac{a^{(I)\alpha*} \left(V_{Hxc}^{(\sigma)} \right)_{(I)m\alpha,(I)m'\alpha'} a^{(I)\alpha'} O^{(I)m'm}}{a^{(I)\alpha''*} a^{(I)\alpha''''} S_{(I)m''\alpha'',(I)m''''\alpha''''} O^{(I)m''m''}}.
\end{aligned}$$

The full derivations of $\bar{V}_{Hxc}^{(I)(\sigma)}$ in the Löwdin representation given in Eq. (48)

$$\begin{aligned}
\bar{V}_{Hxc}^{(I)(\sigma)} &\equiv \frac{Tr[\hat{V}_{Hxc}^{(\sigma)} \hat{P}^{(I)}]}{Tr[\hat{P}^{(I)}]} \\
&= \frac{\sum_{\beta} \langle \phi_{(\beta)} | \hat{V}_{Hxc}^{(\sigma)} | \bar{\phi}_{(I)m\alpha} \rangle \langle \bar{\phi}_{(I)m\alpha} | \phi^{(\beta)} \rangle}{\sum_{\beta'} \langle \phi_{(\beta')} | \bar{\phi}_{(I)m'\alpha'} \rangle \langle \bar{\phi}_{(I)m'\alpha'} | \phi^{(\beta')} \rangle} \\
&= \frac{\sum_{\beta} \langle \phi_{(\beta)} | \hat{V}_{Hxc}^{(\sigma)} | \phi_{\gamma} \rangle \left(S^{-\frac{1}{2}} \right)_{\gamma, (I)m\alpha} \left(S^{-\frac{1}{2}} \right)_{(I)m\alpha, \nu} \langle \phi_{\nu} | \phi^{(\beta)} \rangle}{\sum_{\beta'} \langle \phi_{(\beta')} | \phi_{\gamma'} \rangle \left(S^{-\frac{1}{2}} \right)_{\gamma', (I)m'\alpha'} \left(S^{-\frac{1}{2}} \right)_{(I)m'\alpha', \nu'} \langle \phi_{\nu'} | \phi^{(\beta')} \rangle} \\
&= \frac{\sum_{\beta} \left(V_{Hxc}^{(\sigma)} \right)_{(\beta), \gamma} \left(S^{-\frac{1}{2}} \right)_{\gamma, (I)m\alpha} \left(S^{-\frac{1}{2}} \right)_{(I)m\alpha, \nu} \delta_{\nu}^{(\beta)}}{\sum_{\beta'} S_{(\beta'), \gamma'} \left(S^{-\frac{1}{2}} \right)_{\gamma', (I)m'\alpha'} \left(S^{-\frac{1}{2}} \right)_{(I)m'\alpha', \nu'} \delta_{\nu'}^{(\beta')}} \\
&= \frac{\sum_{m\alpha} \left(S^{-\frac{1}{2}} \right)_{(I)(m)(\alpha), \nu} \left(V_{Hxc}^{(\sigma)} \right)_{\nu, \gamma} \left(S^{-\frac{1}{2}} \right)_{\gamma, (I)(m)(\alpha)}}{\sum_{m'\alpha'} \left(S^{-\frac{1}{2}} \right)_{(I)(m')(\alpha'), \nu'} S_{\nu', \gamma'} \left(S^{-\frac{1}{2}} \right)_{\gamma', (I)(m')(\alpha')}} \\
&= \frac{\sum_{m\alpha} \left(S^{-\frac{1}{2}} V_{Hxc}^{(\sigma)} S^{-\frac{1}{2}} \right)_{(I)(m)(\alpha), (I)(m)(\alpha)}}{\sum_{m'\alpha'} \left(S^{-\frac{1}{2}} S S^{-\frac{1}{2}} \right)_{(I)(m')(\alpha'), (I)(m')(\alpha')}} \\
&= \frac{\sum_{m\alpha} \left(S^{-\frac{1}{2}} V_{Hxc}^{(\sigma)} S^{-\frac{1}{2}} \right)_{(I)(m)(\alpha), (I)(m)(\alpha)}}{|\{m'\}^{(I)}| \cdot |\{\alpha'\}^{(I)}|}.
\end{aligned}$$

7.

Table S1. First-principles linear response U and J parameters for the 3d and 2p subspaces of the representative Ti and O atoms for both the “tensorial” and Löwdin representations. All values are in eV.

parameter	Löwdin	"tensorial"
Ti - U	4.11	3.79
Ti - J	0.38	0.34
O - U	7.45	9.82
O - J	0.76	1.07

9.

Table S2. Calculated linear response U and J values (“tensorial” representation) for the central metal ion (3d subspace) and the representative oxygen atom (2p subspace), together with the standard deviations (“SD – U” or “SD - J”) of the corresponding linear fitting, and the occupation numbers of the 3d subspace of the central metal ion. The U, J and standard deviations are provided in eV.

metal	metal 3d subspace				oxygen 2p subspace				occupation number (metal 3d)	
	U value	SD - U	J value	SD - J	U value	SD - U	J value	SD - J	spin α	spin β
Ti ³⁺	3.37	3.6×10 ⁻⁴	0.39	2.0×10 ⁻⁶	10.40	1.1×10 ⁻⁴	1.59	7.2×10 ⁻⁶	2.09	1.18
V ²⁺	2.60	3.9×10 ⁻⁴	0.45	9.5×10 ⁻⁶	10.71	6.9×10 ⁻⁵	1.48	3.3×10 ⁻⁶	3.50	0.73
Cr ³⁺	3.40	3.4×10 ⁻⁴	0.47	3.2×10 ⁻⁶	10.30	1.2×10 ⁻⁴	1.24	7.7×10 ⁻⁶	3.86	1.23
Cr ²⁺	2.68	3.2×10 ⁻⁴	0.45	8.2×10 ⁻⁷	10.70	7.5×10 ⁻⁵	1.47	3.2×10 ⁻⁶	4.29	0.65
Mn ³⁺	4.50	4.1×10 ⁻⁴	0.53	1.7×10 ⁻⁵	10.14	1.4×10 ⁻⁴	1.14	5.5×10 ⁻⁶	4.47	1.06
Mn ²⁺	3.35	4.7×10 ⁻⁴	0.44	2.8×10 ⁻⁵	10.79	6.6×10 ⁻⁵	1.37	6.0×10 ⁻⁶	4.98	0.48
Fe ³⁺	6.05	4.5×10 ⁻⁴	0.62	9.3×10 ⁻⁶	9.63	2.7×10 ⁻⁴	0.97	1.1×10 ⁻⁵	4.99	1.13
Fe ²⁺	5.13	3.0×10 ⁻⁴	0.50	1.9×10 ⁻⁵	10.54	1.0×10 ⁻⁴	1.25	1.0×10 ⁻⁵	4.99	1.43
Co ³⁺	6.54	2.9×10 ⁻⁴	0.54	5.7×10 ⁻⁶	9.90	9.6×10 ⁻⁵	1.27	3.3×10 ⁻⁶	3.82	3.82
Co ²⁺	5.59	2.6×10 ⁻⁴	0.52	2.1×10 ⁻⁵	10.58	7.4×10 ⁻⁵	1.23	1.0×10 ⁻⁵	4.99	2.40
Ni ²⁺	6.15	2.3×10 ⁻⁴	0.54	1.6×10 ⁻⁵	10.46	9.9×10 ⁻⁵	1.25	8.9×10 ⁻⁶	4.99	3.42
Cu ²⁺	8.10	2.4×10 ⁻⁴	0.99	1.1×10 ⁻⁴	10.74	5.3×10 ⁻⁵	1.34	1.2×10 ⁻⁵	4.98	4.16
Zn ²⁺	-1.65	1.1×10 ⁻⁵	-0.44	2.9×10 ⁻⁷	11.03	6.0×10 ⁻⁵	1.54	2.9×10 ⁻⁶	5.00	5.00

Table S3. Calculated linear response U and J values (Löwdin representation) for the central metal ion (3d subspace) and the representative oxygen atom (2p subspace), together with the standard deviations ("SD - U" or "SD - J") of the corresponding linear fitting, and the occupation numbers of the 3d subspace of the central metal ion. The U, J and standard deviations are provided in eV.

metal	metal 3d subspace				oxygen 2p subspace				occupation number (metal 3d)	
	U	SD - U	J	SD - J	U	SD - U	J	SD - J	spin α	spin β
Ti ³⁺	2.52	3.6×10 ⁻⁵	0.36	1.5×10 ⁻⁶	5.34	8.4×10 ⁻⁵	0.70	9.8×10 ⁻⁶	1.95	1.00
V ²⁺	2.41	4.7×10 ⁻⁵	0.37	2.0×10 ⁻⁶	4.91	4.5×10 ⁻⁵	0.71	9.4×10 ⁻⁶	3.60	0.75
Cr ³⁺	3.39	4.7×10 ⁻⁵	0.43	7.3×10 ⁻⁵	5.66	1.9×10 ⁻⁵	0.72	1.0×10 ⁻⁵	4.06	1.24
Cr ²⁺	3.03	1.5×10 ⁻⁵	0.45	1.0×10 ⁻⁵	5.27	4.0×10 ⁻⁵	0.72	9.7×10 ⁻⁶	4.59	0.79
Mn ³⁺	3.07	1.6×10 ⁻⁵	0.41	5.2×10 ⁻⁶	5.61	9.0×10 ⁻⁵	0.72	1.2×10 ⁻⁵	4.79	1.14
Mn ²⁺	2.41	4.6×10 ⁻⁵	0.38	1.3×10 ⁻⁶	4.88	6.7×10 ⁻⁵	0.73	8.9×10 ⁻⁶	5.39	0.69
Fe ³⁺	3.35	8.6×10 ⁻⁶	0.37	5.0×10 ⁻⁶	6.05	1.9×10 ⁻⁴	0.77	7.4×10 ⁻⁶	5.51	1.33
Fe ²⁺	2.47	4.5×10 ⁻⁵	0.36	1.2×10 ⁻⁶	5.11	5.8×10 ⁻⁵	0.75	8.8×10 ⁻⁶	5.43	1.74
Co ³⁺	5.59	6.3×10 ⁻⁵	0.50	4.1×10 ⁻⁶	5.75	5.0×10 ⁻⁵	0.74	1.1×10 ⁻⁵	4.09	4.09
Co ²⁺	4.93	1.2×10 ⁻⁴	0.49	2.2×10 ⁻⁶	5.38	1.1×10 ⁻⁴	0.77	2.2×10 ⁻⁶	5.41	2.69
Ni ²⁺	2.99	6.6×10 ⁻⁵	0.37	9.0×10 ⁻⁶	5.02	5.0×10 ⁻⁵	0.74	9.7×10 ⁻⁶	5.49	3.79
Cu ²⁺	1.74	2.5×10 ⁻⁵	0.47	3.4×10 ⁻⁵	4.97	8.8×10 ⁻⁵	0.74	2.4×10 ⁻⁶	5.32	4.46
Zn ²⁺	0.61	1.4×10 ⁻⁴	0.24	6.0×10 ⁻⁶	4.88	5.7×10 ⁻⁵	0.69	9.4×10 ⁻⁶	5.48	5.48

10.

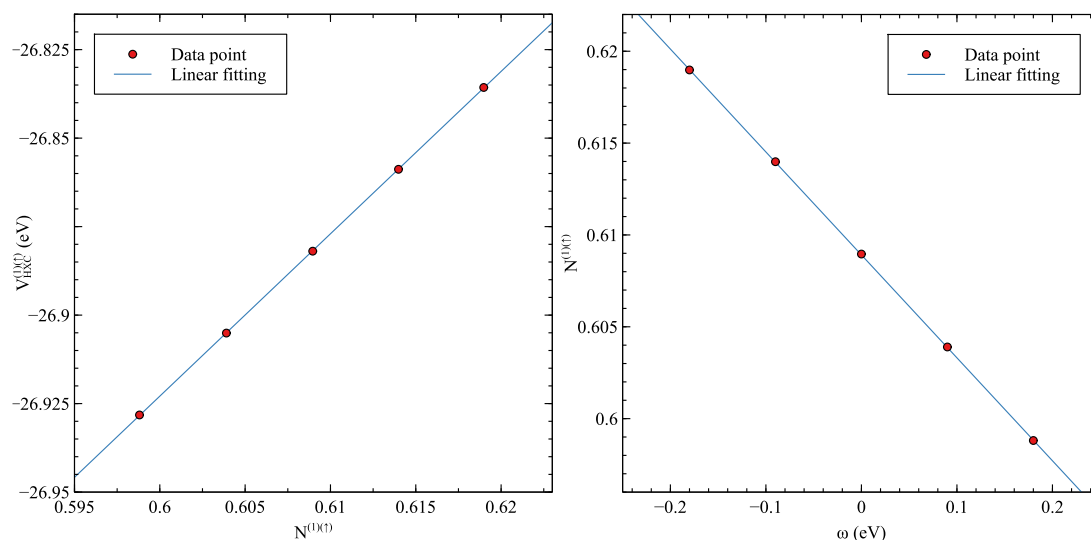
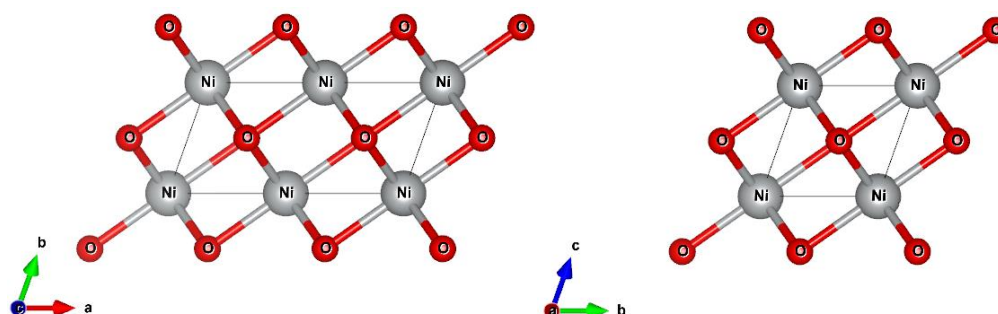
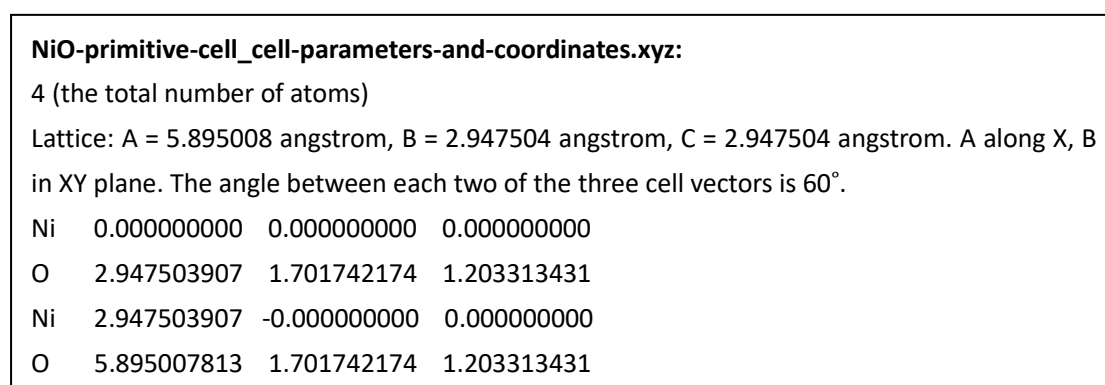


Figure. S1. (Left panel) The data points and their linear fitting for the calculated constrained total occupation number ($N^{(1)(\uparrow)}$) of the $1s$ subspace of the hydrogen atom 1 and the corresponding $V_{Hxc}^{(1)(\uparrow)}$. (Right panel) The data points and their linear fitting for the calculated constrained total occupation number ($N^{(1)(\uparrow)}$) of the $1s$ subspace of the hydrogen atom 1 and the strength ω of the applied constraining potential.

11.



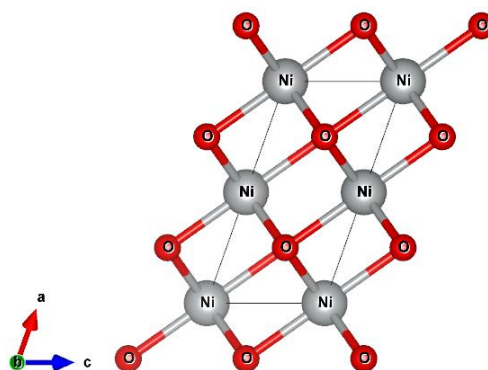


Figure. S2. Views of the NiO primitive cell along the direction of the three lattice vectors.

References

- (1) Hohenberg, P.; Kohn, W. Inhomogeneous Electron Gas. *Phys Rev* **1964**, *136* (3B), B864–B871. <https://doi.org/10.1103/PhysRev.136.B864>.
- (2) Becke, A. D. Perspective: Fifty Years of Density-Functional Theory in Chemical Physics. *J. Chem. Phys.* **2014**, *140* (18), 18A301. <https://doi.org/10.1063/1.4869598>.
- (3) Jones, R. O. Density Functional Theory: Its Origins, Rise to Prominence, and Future. *Rev Mod Phys* **2015**, *87* (3), 897–923. <https://doi.org/10.1103/RevModPhys.87.897>.
- (4) Kohn, W.; Sham, L. J. Self-Consistent Equations Including Exchange and Correlation Effects. *Phys Rev* **1965**, *140* (4A), A1133–A1138. <https://doi.org/10.1103/PhysRev.140.A1133>.
- (5) VandeVondele, J.; Krack, M.; Mohamed, F.; Parrinello, M.; Chassaing, T.; Hutter, J. Quickstep: Fast and Accurate Density Functional Calculations Using a Mixed Gaussian and Plane Waves Approach. *Comput. Phys. Commun.* **2005**, *167* (2), 103–128. <https://doi.org/10.1016/j.cpc.2004.12.014>.
- (6) Kümmel, S.; Kronik, L. Orbital-Dependent Density Functionals: Theory and Applications. *Rev Mod Phys* **2008**, *80* (1), 3–60. <https://doi.org/10.1103/RevModPhys.80.3>.
- (7) Jain, A.; Shin, Y.; Persson, K. A. Computational Predictions of Energy Materials Using Density Functional Theory. *Nat. Rev. Mater.* **2016**, *1* (1), 15004. <https://doi.org/10.1038/natrevmats.2015.4>.
- (8) Malyi, O. I.; Zunger, A. False Metals, Real Insulators, and Degenerate Gapped Metals. *Appl. Phys. Rev.* **2020**, *7* (4), 041310. <https://doi.org/10.1063/5.0015322>.
- (9) Kühne, T. D.; Iannuzzi, M.; Del Ben, M.; Rybkin, V. V.; Seewald, P.; Stein, F.; Laino, T.; Khaliullin, R. Z.; Schütt, O.; Schiffmann, F.; Golze, D.; Wilhelm, J.; Chulkov, S.; Bani-Hashemian, M. H.; Weber, V.; Borštnik, U.; Taillefumier, M.; Jakobovits, A. S.; Lazzaro, A.; Pabst, H.; Müller, T.; Schade, R.; Guidon, M.; Andermatt, S.; Holmberg, N.; Schenter, G. K.; Hehn, A.; Bussy, A.; Belleflamme, F.; Tabacchi, G.; Glöß, A.; Lass, M.; Bethune, I.; Mundy, C. J.; Plessl, C.; Watkins, M.; VandeVondele, J.; Krack, M.; Hutter, J. CP2K: An Electronic Structure and Molecular Dynamics Software Package - Quickstep: Efficient and Accurate Electronic Structure Calculations. *J. Chem. Phys.* **2020**, *152* (19), 194103. <https://doi.org/10.1063/5.0007045>.
- (10) Lippert, G.; Hutter, J.; Parrinello, M. A Hybrid Gaussian and Plane Wave Density Functional

- Scheme. *Mol. Phys.* **1997**, *92* (3), 477–487. <https://doi.org/10.1080/00268979709482119>.
- (11) Vandevondele, J. *CP2K: Overview and Summary of New Features*; First Annual CP2K UK Users Meeting; University of London, 2014.
- (12) Vandevondele, J.; Borštnik, U.; Hutter, J. Linear Scaling Self-Consistent Field Calculations with Millions of Atoms in the Condensed Phase. *J. Chem. Theory Comput.* **2012**, *8* (10), 3565–3573. <https://doi.org/10.1021/ct200897x>.
- (13) Perdew, J. P.; Zunger, A. Self-Interaction Correction to Density-Functional Approximations for Many-Electron Systems. *Phys Rev B* **1981**, *23* (10), 5048–5079. <https://doi.org/10.1103/PhysRevB.23.5048>.
- (14) Zhang, Y.; Yang, W. A Challenge for Density Functionals: Self-Interaction Error Increases for Systems with a Noninteger Number of Electrons. *J. Chem. Phys.* **1998**, *109* (7), 2604–2608. <https://doi.org/10.1063/1.476859>.
- (15) Cohen Aron J.; Mori-Sánchez Paula; Yang Weitao. Insights into Current Limitations of Density Functional Theory. *Science* **2008**, *321* (5890), 792–794. <https://doi.org/10.1126/science.1158722>.
- (16) Mori-Sánchez, P.; Cohen, A. J.; Yang, W. Many-Electron Self-Interaction Error in Approximate Density Functionals. *J. Chem. Phys.* **2006**, *125* (20), 201102. <https://doi.org/10.1063/1.2403848>.
- (17) Ruzsinszky, A.; Perdew, J. P.; Csonka, G. I.; Vydrov, O. A.; Scuseria, G. E. Density Functionals That Are One- and Two- Are Not Always Many-Electron Self-Interaction-Free, as Shown for H_2^+ , He_2^+ , LiH^+ , and Ne_2^+ . *J. Chem. Phys.* **2007**, *126* (10), 104102. <https://doi.org/10.1063/1.2566637>.
- (18) Perdew, J. P.; Parr, R. G.; Levy, M.; Balduz, J. L. Density-Functional Theory for Fractional Particle Number: Derivative Discontinuities of the Energy. *Phys Rev Lett* **1982**, *49* (23), 1691–1694. <https://doi.org/10.1103/PhysRevLett.49.1691>.
- (19) Anisimov, V. I.; Poteryaev, A. I.; Korotin, M. A.; Anokhin, A. O.; Kotliar, G. First-Principles Calculations of the Electronic Structure and Spectra of Strongly Correlated Systems: Dynamical Mean-Field Theory. *J. Phys. Condens. Matter* **1997**, *9* (35), 7359–7367. <https://doi.org/10.1088/0953-8984/9/35/010>.
- (20) Pacchioni, G. Modeling Doped and Defective Oxides in Catalysis with Density Functional Theory Methods: Room for Improvements. *J. Chem. Phys.* **2008**, *128* (18), 182505. <https://doi.org/10.1063/1.2819245>.
- (21) Ganduglia-Pirovano, M. V.; Hofmann, A.; Sauer, J. Oxygen Vacancies in Transition Metal and Rare Earth Oxides: Current State of Understanding and Remaining Challenges. *Surf. Sci. Rep.* **2007**, *62* (6), 219–270. <https://doi.org/10.1016/j.surfrep.2007.03.002>.
- (22) Mikami, M.; Nakamura, S.; Kitao, O.; Arakawa, H.; Gonze, X. First-Principles Study of Titanium Dioxide: Rutile and Anatase. *Jpn. J. Appl. Phys.* **2000**, *39* (Part 2, No. 8B), L847–L850. <https://doi.org/10.1143/jjap.39.L847>.
- (23) Huang, P.; Carter, E. A. Advances in Correlated Electronic Structure Methods for Solids, Surfaces, and Nanostructures. *Annu. Rev. Phys. Chem.* **2008**, *59* (1), 261–290. <https://doi.org/10.1146/annurev.physchem.59.032607.093528>.
- (24) Droghetti, A.; Rungger, I.; Das Pemmaraju, C.; Sanvito, S. Fundamental Gap of Molecular Crystals via Constrained Density Functional Theory. *Phys Rev B* **2016**, *93* (19), 195208. <https://doi.org/10.1103/PhysRevB.93.195208>.

- (25) Linscott, E. B.; Cole, D. J.; Payne, M. C.; O'Regan, D. D. Role of Spin in the Calculation of Hubbard U and Hund's J Parameters from First Principles. *Phys Rev B* **2018**, *98* (23), 235157. <https://doi.org/10.1103/PhysRevB.98.235157>.
- (26) Orhan, O. K.; O'Regan, D. D. First-Principles Hubbard U and Hund's J Corrected Approximate Density Functional Theory Predicts an Accurate Fundamental Gap in Rutile and Anatase TiO_2 . *Phys. Rev. B* **2020**, *101* (24), 245137. <https://doi.org/10.1103/PhysRevB.101.245137>.
- (27) Lambert, D. S.; O'Regan, D. D. Use of $DFT+U+J$ with Linear Response Parameters to Predict Non-Magnetic Oxide Band Gaps with Hybrid-Functional Accuracy. *Phys Rev Res* **2023**, *5* (1), 013160. <https://doi.org/10.1103/PhysRevResearch.5.013160>.
- (28) Pederson, M. R.; Ruzsinszky, A.; Perdew, J. P. Communication: Self-Interaction Correction with Unitary Invariance in Density Functional Theory. *J. Chem. Phys.* **2014**, *140* (12), 121103. <https://doi.org/10.1063/1.4869581>.
- (29) Pederson, M. R. Fermi Orbital Derivatives in Self-Interaction Corrected Density Functional Theory: Applications to Closed Shell Atoms. *J. Chem. Phys.* **2015**, *142* (6), 064112. <https://doi.org/10.1063/1.4907592>.
- (30) Hahn, T.; Liebing, S.; Kortus, J.; Pederson, M. R. Fermi Orbital Self-Interaction Corrected Electronic Structure of Molecules beyond Local Density Approximation. *J. Chem. Phys.* **2015**, *143* (22), 224104. <https://doi.org/10.1063/1.4936777>.
- (31) Dabo, I.; Ferretti, A.; Poilvert, N.; Li, Y.; Marzari, N.; Cococcioni, M. Koopmans' Condition for Density-Functional Theory. *Phys. Rev. B* **2010**, *82* (11), 115121. <https://doi.org/10.1103/PhysRevB.82.115121>.
- (32) Borghi, G.; Ferretti, A.; Nguyen, N. L.; Dabo, I.; Marzari, N. Koopmans-Compliant Functionals and Their Performance against Reference Molecular Data. *Phys Rev B* **2014**, *90* (7), 075135. <https://doi.org/10.1103/PhysRevB.90.075135>.
- (33) Metzner, W.; Vollhardt, D. Correlated Lattice Fermions in $d=\infty$ Dimensions. *Phys Rev Lett* **1989**, *62* (3), 324–327. <https://doi.org/10.1103/PhysRevLett.62.324>.
- (34) Müller-Hartmann, E. Correlated Fermions on a Lattice in High Dimensions. *Z. Für Phys. B Condens. Matter* **1989**, *74* (4), 507–512. <https://doi.org/10.1007/BF01311397>.
- (35) Brandt, U.; Mielsch, C. Thermodynamics and Correlation Functions of the Falicov-Kimball Model in Large Dimensions. *Z. Für Phys. B Condens. Matter* **1989**, *75* (3), 365–370. <https://doi.org/10.1007/BF01321824>.
- (36) Janiš, V. A New Construction of Thermodynamic Mean-Field Theories of Itinerant Fermions: Application to the Falicov-Kimball Model. *Z. Für Phys. B Condens. Matter* **1991**, *83* (2), 227–235. <https://doi.org/10.1007/BF01309423>.
- (37) Georges, A.; Kotliar, G. Hubbard Model in Infinite Dimensions. *Phys Rev B* **1992**, *45* (12), 6479–6483. <https://doi.org/10.1103/PhysRevB.45.6479>.
- (38) Georges, A.; Kotliar, G.; Krauth, W.; Rozenberg, M. J. Dynamical Mean-Field Theory of Strongly Correlated Fermion Systems and the Limit of Infinite Dimensions. *Rev Mod Phys* **1996**, *68* (1), 13–125. <https://doi.org/10.1103/RevModPhys.68.13>.
- (39) Pavarini, E.; Vollhardt, D.; Koch, E.; Lichtenstein, A. *The LDA+ DMFT Approach to Strongly Correlated Materials*; Theoretische Nanoelektronik, 2011.
- (40) Himmetoglu, B.; Floris, A.; de Gironcoli, S.; Cococcioni, M. Hubbard-Corrected DFT Energy Functionals: The LDA+ U Description of Correlated Systems. *Int. J. Quantum Chem.* **2014**,

- 114 (1), 14–49. <https://doi.org/10.1002/qua.24521>.
- (41) Hedin, L. New Method for Calculating the One-Particle Green's Function with Application to the Electron-Gas Problem. *Phys. Rev.* **1965**, *139* (3A), A796–A823. <https://doi.org/10.1103/PhysRev.139.A796>.
- (42) Hybertsen, M. S.; Louie, S. G. Electron Correlation in Semiconductors and Insulators: Band Gaps and Quasiparticle Energies. *Phys. Rev. B* **1986**, *34* (8), 5390–5413. <https://doi.org/10.1103/PhysRevB.34.5390>.
- (43) Aryasetiawan, F.; Gunnarsson, O. The GW method. *Rep. Prog. Phys.* **1998**, *61* (3), 237–312. <https://doi.org/10.1088/0034-4885/61/3/002>.
- (44) Golze, D.; Dvorak, M.; Rinke, P. The GW Compendium: A Practical Guide to Theoretical Photoemission Spectroscopy. *Front. Chem.* **2019**, *7*, 377. <https://doi.org/10.3389/fchem.2019.00377>.
- (45) Heinemann, M.; Eifert, B.; Heiliger, C. Band Structure and Phase Stability of the Copper Oxides Cu₂O, CuO, and Cu₄O₃. *Phys Rev B* **2013**, *87* (11), 115111. <https://doi.org/10.1103/PhysRevB.87.115111>.
- (46) Peng, H.; Perdew, J. P. Synergy of van Der Waals and Self-Interaction Corrections in Transition Metal Monoxides. *Phys Rev B* **2017**, *96* (10), 100101. <https://doi.org/10.1103/PhysRevB.96.100101>.
- (47) Ghosh, A.; Jana, S.; Niranjana, M. K.; Tran, F.; Wimberger, D.; Blaha, P.; Constantin, L. A.; Samal, P. Correct and Accurate Polymorphic Energy Ordering of Transition-Metal Monoxides Obtained from Semilocal and Onsite-Hybrid Exchange-Correlation Approximations. **2021**.
- (48) Anisimov, V. I.; Gunnarsson, O. Density-Functional Calculation of Effective Coulomb Interactions in Metals. *Phys Rev B* **1991**, *43* (10), 7570–7574. <https://doi.org/10.1103/PhysRevB.43.7570>.
- (49) Anisimov, V. I.; Zaanen, J.; Andersen, O. K. Band Theory and Mott Insulators: Hubbard U Instead of Stoner I. *Phys Rev B* **1991**, *44* (3), 943–954. <https://doi.org/10.1103/PhysRevB.44.943>.
- (50) Anisimov, V. I.; Solovyev, I. V.; Korotin, M. A.; Czyżyk, M. T.; Sawatzky, G. A. Density-Functional Theory and NiO Photoemission Spectra. *Phys Rev B* **1993**, *48* (23), 16929–16934. <https://doi.org/10.1103/PhysRevB.48.16929>.
- (51) Czyżyk, M. T.; Sawatzky, G. A. Local-Density Functional and on-Site Correlations: The Electronic Structure of La₂CuO₄ and LaCuO₃. *Phys Rev B* **1994**, *49* (20), 14211–14228. <https://doi.org/10.1103/PhysRevB.49.14211>.
- (52) Solovyev, I. V.; Dederichs, P. H.; Anisimov, V. I. Corrected Atomic Limit in the Local-Density Approximation and the Electronic Structure of d Impurities in Rb. *Phys Rev B* **1994**, *50* (23), 16861–16871. <https://doi.org/10.1103/PhysRevB.50.16861>.
- (53) Liechtenstein, A. I.; Anisimov, V. I.; Zaanen, J. Density-Functional Theory and Strong Interactions: Orbital Ordering in Mott-Hubbard Insulators. *Phys Rev B* **1995**, *52* (8), R5467–R5470. <https://doi.org/10.1103/PhysRevB.52.R5467>.
- (54) Pickett, W. E.; Erwin, S. C.; Ethridge, E. C. Reformulation of the LDA+*U* Method for a Local-Orbital Basis. *Phys Rev B* **1998**, *58* (3), 1201–1209. <https://doi.org/10.1103/PhysRevB.58.1201>.
- (55) Cococcioni, M.; de Gironcoli, S. Linear Response Approach to the Calculation of the

- Effective Interaction Parameters in the LDA+U Method. *Phys Rev B* **2005**, *71* (3), 035105. <https://doi.org/10.1103/PhysRevB.71.035105>.
- (56) Kulik, H. J.; Cococcioni, M.; Scherlis, D. A.; Marzari, N. Density Functional Theory in Transition-Metal Chemistry: A Self-Consistent Hubbard U Approach. *Phys Rev Lett* **2006**, *97* (10), 103001. <https://doi.org/10.1103/PhysRevLett.97.103001>.
- (57) Zhao, Q.; Ioannidis, E. I.; Kulik, H. J. Global and Local Curvature in Density Functional Theory. *J. Chem. Phys.* **2016**, *145* (5), 054109. <https://doi.org/10.1063/1.4959882>.
- (58) Dudarev, S. L.; Botton, G. A.; Savrasov, S. Y.; Humphreys, C. J.; Sutton, A. P. Electron-Energy-Loss Spectra and the Structural Stability of Nickel Oxide: An LSDA+U Study. *Phys Rev B* **1998**, *57* (3), 1505–1509. <https://doi.org/10.1103/PhysRevB.57.1505>.
- (59) Anisimov, V. I.; Aryasetiawan, F.; Lichtenstein, A. I. First-Principles Calculations of the Electronic Structure and Spectra of Strongly Correlated Systems: The LDA+ U Method. *J. Phys. Condens. Matter* **1997**, *9* (4), 767–808. <https://doi.org/10.1088/0953-8984/9/4/002>.
- (60) Mosey, N. J.; Carter, E. A. Ab Initio Evaluation of Coulomb and Exchange Parameters for DFT+U Calculations. *Phys Rev B* **2007**, *76* (15), 155123. <https://doi.org/10.1103/PhysRevB.76.155123>.
- (61) Himmetoglu, B.; Wentzcovitch, R. M.; Cococcioni, M. First-Principles Study of Electronic and Structural Properties of CuO. *Phys Rev B* **2011**, *84* (11), 115108. <https://doi.org/10.1103/PhysRevB.84.115108>.
- (62) Shishkin, M.; Sato, H. Evaluation of Redox Potentials of Cathode Materials of Alkali-Ion Batteries Using Extended DFT+U+ $U\uparrow\downarrow$ Method: The Role of Interactions between the Electrons with Opposite Spins. *J. Chem. Phys.* **2021**, *154* (11), 114709. <https://doi.org/10.1063/5.0039594>.
- (63) Soler-Polo, D.; Ortega, J.; Flores, F. A Local-Orbital Density Functional Formalism for a Many-Body Atomic Hamiltonian: Hubbard–Hund’s Coupling and DFT + U Functional. *J. Phys. Condens. Matter* **2021**, *33* (42), 425604. <https://doi.org/10.1088/1361-648x/ac1155>.
- (64) Moynihan, G. A Self-Contained Ground-State Approach for the Correction of Self-Interaction Error in Approximate Density-Functional Theory. Ph.D. thesis, School of Physics, Trinity College Dublin, 2018.
- (65) Rohrbach, A.; Hafner, J.; Kresse, G. Ab Initio Study of the (0001) Surfaces of Hematite and Chromia: Influence of Strong Electronic Correlations. *Phys Rev B* **2004**, *70* (12), 125426. <https://doi.org/10.1103/PhysRevB.70.125426>.
- (66) Morgan, B. J.; Watson, G. W. A DFT+U Description of Oxygen Vacancies at the TiO₂ Rutile (110) Surface. *Surf. Sci.* **2007**, *601* (21), 5034–5041. <https://doi.org/10.1016/j.susc.2007.08.025>.
- (67) Castleton, C. W. M.; Kullgren, J.; Hermansson, K. Tuning LDA+U for Electron Localization and Structure at Oxygen Vacancies in Ceria. *J. Chem. Phys.* **2007**, *127* (24), 244704. <https://doi.org/10.1063/1.2800015>.
- (68) Loschen, C.; Carrasco, J.; Neyman, K. M.; Illas, F. First-Principles LDA+U and GGA+U Study of Cerium Oxides: Dependence on the Effective U Parameter. *Phys Rev B* **2007**, *75* (3), 035115. <https://doi.org/10.1103/PhysRevB.75.035115>.
- (69) Wang, L.; Maxisch, T.; Ceder, G. Oxidation Energies of Transition Metal Oxides within the GGA+U Framework. *Phys Rev B* **2006**, *73* (19), 195107. <https://doi.org/10.1103/PhysRevB.73.195107>.

- (70) Ong, S. P.; Chevrier, V. L.; Hautier, G.; Jain, A.; Moore, C.; Kim, S.; Ma, X.; Ceder, G. Voltage, Stability and Diffusion Barrier Differences between Sodium-Ion and Lithium-Ion Intercalation Materials. *Energy Environ. Sci.* **2011**, *4* (9), 3680–3688. <https://doi.org/10.1039/C1EE01782A>.
- (71) Gunnarsson, O. Calculation of Parameters in Model Hamiltonians. *Phys Rev B* **1990**, *41* (1), 514–518. <https://doi.org/10.1103/PhysRevB.41.514>.
- (72) Solovyev, I. V.; Dederichs, P. H. Ab Initio Calculations of Coulomb U Parameters for Transition-Metal Impurities. *Phys Rev B* **1994**, *49* (10), 6736–6740. <https://doi.org/10.1103/PhysRevB.49.6736>.
- (73) Gunnarsson, O.; Andersen, O. K.; Jepsen, O.; Zaanen, J. Density-Functional Calculation of the Parameters in the Anderson Model: Application to Mn in CdTe. *Phys Rev B* **1989**, *39* (3), 1708–1722. <https://doi.org/10.1103/PhysRevB.39.1708>.
- (74) Dederichs, P. H.; Blügel, S.; Zeller, R.; Akai, H. Ground States of Constrained Systems: Application to Cerium Impurities. *Phys Rev Lett* **1984**, *53* (26), 2512–2515. <https://doi.org/10.1103/PhysRevLett.53.2512>.
- (75) McMahan, A. K.; Martin, R. M.; Satpathy, S. Calculated Effective Hamiltonian for La₂CuO₄ and Solution in the Impurity Anderson Approximation. *Phys Rev B* **1988**, *38* (10), 6650–6666. <https://doi.org/10.1103/PhysRevB.38.6650>.
- (76) Hybertsen, M. S.; Schlüter, M.; Christensen, N. E. Calculation of Coulomb-Interaction Parameters for La₂CuO₄ Using a Constrained-Density-Functional Approach. *Phys Rev B* **1989**, *39* (13), 9028–9041. <https://doi.org/10.1103/PhysRevB.39.9028>.
- (77) Solovyev, I. V.; Imada, M. Screening of Coulomb Interactions in Transition Metals. *Phys Rev B* **2005**, *71* (4), 045103. <https://doi.org/10.1103/PhysRevB.71.045103>.
- (78) Vaugier, L.; Jiang, H.; Biermann, S. Hubbard U and Hund Exchange J in Transition Metal Oxides: Screening versus Localization Trends from Constrained Random Phase Approximation. *Phys Rev B* **2012**, *86* (16), 165105. <https://doi.org/10.1103/PhysRevB.86.165105>.
- (79) Springer, M.; Aryasetiawan, F. Frequency-Dependent Screened Interaction in Ni within the Random-Phase Approximation. *Phys Rev B* **1998**, *57* (8), 4364–4368. <https://doi.org/10.1103/PhysRevB.57.4364>.
- (80) Aryasetiawan, F.; Imada, M.; Georges, A.; Kotliar, G.; Biermann, S.; Lichtenstein, A. I. Frequency-Dependent Local Interactions and Low-Energy Effective Models from Electronic Structure Calculations. *Phys Rev B* **2004**, *70* (19), 195104. <https://doi.org/10.1103/PhysRevB.70.195104>.
- (81) Aryasetiawan, F.; Karlsson, K.; Jepsen, O.; Schönberger, U. Calculations of Hubbard U from First-Principles. *Phys Rev B* **2006**, *74* (12), 125106. <https://doi.org/10.1103/PhysRevB.74.125106>.
- (82) Şaşıoğlu, E.; Friedrich, C.; Blügel, S. Strength of the Effective Coulomb Interaction at Metal and Insulator Surfaces. *Phys Rev Lett* **2012**, *109* (14), 146401. <https://doi.org/10.1103/PhysRevLett.109.146401>.
- (83) MacEnulty, L.; O'Regan, D. D. Optimization Strategies Developed on NiO for Heisenberg Exchange Coupling Calculations Using Projector Augmented Wave Based First-Principles DFT+ U + J . *Phys. Rev. B* **2023**, *108* (24), 245137. <https://doi.org/10.1103/PhysRevB.108.245137>.

- (84) Moynihan, G.; Teobaldi, G.; O'Regan, D. D. A Self-Consistent Ground-State Formulation of the First-Principles Hubbard U Parameter Validated on One-Electron Self-Interaction Error. **2017**.
- (85) Prentice, J. C. A.; Aarons, J.; Womack, J. C.; Allen, A. E. A.; Andrinopoulos, L.; Anton, L.; Bell, R. A.; Bhandari, A.; Bramley, G. A.; Charlton, R. J.; Clements, R. J.; Cole, D. J.; Constantinescu, G.; Corsetti, F.; Dubois, S. M.-M.; Duff, K. K. B.; Escartín, J. M.; Greco, A.; Hill, Q.; Lee, L. P.; Linscott, E.; O'Regan, D. D.; Phipps, M. J. S.; Ratcliff, L. E.; Serrano, Á. R.; Tait, E. W.; Teobaldi, G.; Vitale, V.; Yeung, N.; Zuehlsdorff, T. J.; Dziedzic, J.; Haynes, P. D.; Hine, N. D. M.; Mostofi, A. A.; Payne, M. C.; Skylaris, C.-K. The ONETEP Linear-Scaling Density Functional Theory Program. *J. Chem. Phys.* **2020**, *152* (17), 174111. <https://doi.org/10.1063/5.0004445>.
- (86) García, A.; Papior, N.; Akhtar, A.; Artacho, E.; Blum, V.; Bosoni, E.; Brandimarte, P.; Brandbyge, M.; Cerdá, J. I.; Corsetti, F.; Cuadrado, R.; Dikan, V.; Ferrer, J.; Gale, J.; García-Fernández, P.; García-Suárez, V. M.; García, S.; Huhs, G.; Illera, S.; Korytár, R.; Koval, P.; Lebedeva, I.; Lin, L.; López-Tarifa, P.; Mayo, S. G.; Mohr, S.; Ordejón, P.; Postnikov, A.; Pouillon, Y.; Pruneda, M.; Robles, R.; Sánchez-Portal, D.; Soler, J. M.; Ullah, R.; Yu, V. W.; Junquera, J. Siesta: Recent Developments and Applications. *J. Chem. Phys.* **2020**, *152* (20), 204108. <https://doi.org/10.1063/5.0005077>.
- (87) Han, M. J.; Ozaki, T.; Yu, J. $O(N)$ LDA+ U electronic structure calculation method based on the nonorthogonal pseudoatomic orbital basis *Phys Rev B* **2006**, *73* (4), 045110. <https://doi.org/10.1103/PhysRevB.73.045110>.
- (88) Ryee, S.; Han, M. J. Comparative Study of DFT+ U Functionals for Non-Collinear Magnetism. *J. Phys. Condens. Matter* **2018**, *30* (27), 275802. <https://doi.org/10.1088/1361-648x/aac79c>.
- (89) Ryee, S.; Han, M. J. The Effect of Double Counting, Spin Density, and Hund Interaction in the Different DFT+ U Functionals. *Sci. Rep.* **2018**, *8* (1), 9559. <https://doi.org/10.1038/s41598-018-27731-4>.
- (90) Ryee, S. *DFT+U Modified Code Description*. http://www.openmx-square.org/tech_notes/tech6-1_0.pdf.
- (91) Ozaki, T. *LDA+U Method: Ver. 1.0*; RCIS, JAIST, 2007. http://www.openmx-square.org/tech_notes/DFTU_notes_OpenMX.pdf.
- (92) Giannozzi, P.; Andreussi, O.; Brumme, T.; Bunau, O.; Buongiorno Nardelli, M.; Calandra, M.; Car, R.; Cavazzoni, C.; Ceresoli, D.; Cococcioni, M.; Colonna, N.; Carneiro, I.; Dal Corso, A.; de Gironcoli, S.; Delugas, P.; DiStasio, R. A.; Ferretti, A.; Floris, A.; Fratesi, G.; Fugallo, G.; Gebauer, R.; Gerstmann, U.; Giustino, F.; Gorni, T.; Jia, J.; Kawamura, M.; Ko, H.-Y.; Kokalj, A.; Küçükbenli, E.; Lazzeri, M.; Marsili, M.; Marzari, N.; Mauri, F.; Nguyen, N. L.; Nguyen, H.-V.; Otero-de-la-Roza, A.; Paulatto, L.; Poncé, S.; Rocca, D.; Sabatini, R.; Santra, B.; Schlipf, M.; Seitsonen, A. P.; Smogunov, A.; Timrov, I.; Thonhauser, T.; Umari, P.; Vast, N.; Wu, X.; Baroni, S. Advanced Capabilities for Materials Modelling with Quantum ESPRESSO. *J. Phys. Condens. Matter* **2017**, *29* (46), 465901. <https://doi.org/10.1088/1361-648X/aa8f79>.
- (93) Timrov, I.; Aquilante, F.; Binci, L.; Cococcioni, M.; Marzari, N. Pulay Forces in Density-Functional Theory with Extended Hubbard Functionals: From Nonorthogonalized to Orthogonalized Manifolds. *Phys Rev B* **2020**, *102* (23), 235159. <https://doi.org/10.1103/PhysRevB.102.235159>.

- (94) Rohrbach, A.; Hafner, J.; Kresse, G. Electronic Correlation Effects in Transition-Metal Sulfides. *J. Phys. Condens. Matter* **2003**, *15* (6), 979–996. <https://doi.org/10.1088/0953-8984/15/6/325>.
- (95) Bengone, O.; Alouani, M.; Blöchl, P.; Hugel, J. Implementation of the Projector Augmented-Wave LDA+U Method: Application to the Electronic Structure of NiO. *Phys Rev B* **2000**, *62* (24), 16392–16401. <https://doi.org/10.1103/PhysRevB.62.16392>.
- (96) Amadon, B.; Jollet, F.; Torrent, M. γ and β Cerium: LDA+U Calculations of Ground-State Parameters. *Phys Rev B* **2008**, *77* (15), 155104. <https://doi.org/10.1103/PhysRevB.77.155104>.
- (97) Kick, M.; Reuter, K.; Oberhofer, H. Intricacies of DFT+U, Not Only in a Numeric Atom Centered Orbital Framework. *J. Chem. Theory Comput.* **2019**, *15* (3), 1705–1718. <https://doi.org/10.1021/acs.jctc.8b01211>.
- (98) Nakata, A.; Baker, J. S.; Mujahed, S. Y.; Poulton, J. T. L.; Arapan, S.; Lin, J.; Raza, Z.; Yadav, S.; Truflandier, L.; Miyazaki, T.; Bowler, D. R. Large Scale and Linear Scaling DFT with the CONQUEST Code. *J. Chem. Phys.* **2020**, *152* (16), 164112. <https://doi.org/10.1063/5.0005074>.
- (99) Tablero, C. Representations of the Occupation Number Matrix on the LDA/GGA+U method. *J. Phys. Condens. Matter* **2008**, *20* (32), 325205. <https://doi.org/10.1088/0953-8984/20/32/325205>.
- (100) Eschrig, H.; Koepnick, K.; Chaplygin, I. Density Functional Application to Strongly Correlated Electron Systems. *Spec. Issue Impact Theor. Methods Solid-State Chem.* **2003**, *176* (2), 482–495. [https://doi.org/10.1016/S0022-4596\(03\)00274-3](https://doi.org/10.1016/S0022-4596(03)00274-3).
- (101) O'Regan, D. D.; Payne, M. C.; Mostofi, A. A. Subspace Representations in Ab Initio Methods for Strongly Correlated Systems. *Phys Rev B* **2011**, *83* (24), 245124. <https://doi.org/10.1103/PhysRevB.83.245124>.
- (102) O'Regan, D. D. *Optimised Projections for the Ab Initio Simulation of Large and Strongly Correlated Systems*; Springer Berlin Heidelberg: Berlin, Heidelberg, 2012. <https://doi.org/10.1007/978-3-642-23238-1>.
- (103) O'Regan, D. D.; Hine, N. D. M.; Payne, M. C.; Mostofi, A. A. Projector Self-Consistent DFT+U Using Nonorthogonal Generalized Wannier Functions. *Phys Rev B* **2010**, *82* (8), 081102. <https://doi.org/10.1103/PhysRevB.82.081102>.
- (104) Leiria Campo Jr, V.; Cococcioni, M. Extended DFT +U+V method with On-Site and Inter-Site Electronic Interactions. *J. Phys. Condens. Matter* **2010**, *22* (5), 055602. <https://doi.org/10.1088/0953-8984/22/5/055602>.
- (105) Timrov, I.; Marzari, N.; Cococcioni, M. Self-Consistent Hubbard Parameters from Density-Functional Perturbation Theory in the Ultrasoft and Projector-Augmented Wave Formulations. *Phys Rev B* **2021**, *103* (4), 045141. <https://doi.org/10.1103/PhysRevB.103.045141>.
- (106) Agapito, L. A.; Curtarolo, S.; Buongiorno Nardelli, M. Reformulation of DFT+U as a Pseudohybrid Hubbard Density Functional for Accelerated Materials Discovery. *Phys Rev X* **2015**, *5* (1), 011006. <https://doi.org/10.1103/PhysRevX.5.011006>.
- (107) Shishkin, M.; Sato, H. Self-Consistent Parametrization of DFT + U Framework Using Linear Response Approach: Application to Evaluation of Redox Potentials of Battery Cathodes. *Phys Rev B* **2016**, *93* (8), 085135. <https://doi.org/10.1103/PhysRevB.93.085135>.

- (108) Einstein, A. Die Grundlage Der Allgemeinen Relativitätstheorie. *Ann. Phys.* **1916**, 354 (7), 769–822. <https://doi.org/10.1002/andp.19163540702>.
- (109) https://Manual.Cp2k.Org/Cp2k-2023_1-Branch/CP2K_INPUT/FORCE_EVAL/DFT.html#PLUS_U_METHOD.
- (110) https://Github.Com/Cp2k/Cp2k/Blob/Master/Src/Ct_methods.F.
- (111) Svane, A.; Gunnarsson, O. Transition-Metal Oxides in the Self-Interaction–Corrected Density-Functional Formalism. *Phys Rev Lett* **1990**, 65 (9), 1148–1151. <https://doi.org/10.1103/PhysRevLett.65.1148>.
- (112) Shen, Z.-X.; List, R. S.; Dessau, D. S.; Wells, B. O.; Jepsen, O.; Arko, A. J.; Bartlett, R.; Shih, C. K.; Parmigiani, F.; Huang, J. C.; Lindberg, P. A. P. Electronic Structure of NiO: Correlation and Band Effects. *Phys Rev B* **1991**, 44 (8), 3604–3626. <https://doi.org/10.1103/PhysRevB.44.3604>.
- (113) Terakura, K.; Oguchi, T.; Williams, A. R.; Kübler, J. Band Theory of Insulating Transition-Metal Monoxides: Band-Structure Calculations. *Phys Rev B* **1984**, 30 (8), 4734–4747. <https://doi.org/10.1103/PhysRevB.30.4734>.
- (114) Bredow, T.; Gerson, A. R. Effect of Exchange and Correlation on Bulk Properties of MgO, NiO, and CoO. *Phys Rev B* **2000**, 61 (8), 5194–5201. <https://doi.org/10.1103/PhysRevB.61.5194>.
- (115) Petukhov, A. G.; Mazin, I. I.; Chioncel, L.; Lichtenstein, A. I. Correlated Metals and the LDA+*U* Method. *Phys Rev B* **2003**, 67 (15), 153106. <https://doi.org/10.1103/PhysRevB.67.153106>.
- (116) Jiang, H.; Gomez-Abal, R. I.; Rinke, P.; Scheffler, M. First-Principles Modeling of Localized *d* States with the *GW@LDA+U* Approach. *Phys Rev B* **2010**, 82 (4), 045108. <https://doi.org/10.1103/PhysRevB.82.045108>.
- (117) Park, S. Y.; Choi, H. J. First-Principles Calculation of Atomic Force in the LSDA+*U* Formalism. *Phys Rev B* **2009**, 80 (15), 155122. <https://doi.org/10.1103/PhysRevB.80.155122>.
- (118) Szotek, Z.; Temmerman, W. M.; Winter, H. Application of the Self-Interaction Correction to Transition-Metal Oxides. *Phys Rev B* **1993**, 47 (7), 4029–4032. <https://doi.org/10.1103/PhysRevB.47.4029>.
- (119) Arai, M.; Fujiwara, T. Electronic Structures of Transition-Metal Mono-Oxides in the Self-Interaction-Corrected Local-Spin-Density Approximation. *Phys Rev B* **1995**, 51 (3), 1477–1489. <https://doi.org/10.1103/PhysRevB.51.1477>.
- (120) Aryasetiawan, F.; Gunnarsson, O. Electronic Structure of NiO in the *GW* Approximation. *Phys Rev Lett* **1995**, 74 (16), 3221–3224. <https://doi.org/10.1103/PhysRevLett.74.3221>.
- (121) Faleev, S. V.; van Schilfhaarde, M.; Kotani, T. All-Electron Self-Consistent $\$GW\$$ Approximation: Application to Si, MnO, and NiO. *Phys Rev Lett* **2004**, 93 (12), 126406. <https://doi.org/10.1103/PhysRevLett.93.126406>.
- (122) Li, J.-L.; Rignanese, G.-M.; Louie, S. G. Quasiparticle Energy Bands of NiO in the G_{0W} Approximation. *Phys Rev B* **2005**, 71 (19), 193102. <https://doi.org/10.1103/PhysRevB.71.193102>.
- (123) Kobayashi, S.; Nohara, Y.; Yamamoto, S.; Fujiwara, T. *GW* Approximation with LSDA+*U* Method and Applications to NiO, MnO, and V₂O₃. *Phys Rev B* **2008**, 78 (15), 155112. <https://doi.org/10.1103/PhysRevB.78.155112>.
- (124) Ren, X.; Leonov, I.; Keller, G.; Kollar, M.; Nekrasov, I.; Vollhardt, D. LDA+DMFT Computation

- of the Electronic Spectrum of NiO. *Phys Rev B* **2006**, *74* (19), 195114. <https://doi.org/10.1103/PhysRevB.74.195114>.
- (125) Kuneš, J.; Anisimov, V. I.; Lukoyanov, A. V.; Vollhardt, D. Local Correlations and Hole Doping in NiO: A Dynamical Mean-Field Study. *Phys Rev B* **2007**, *75* (16), 165115. <https://doi.org/10.1103/PhysRevB.75.165115>.
- (126) Yin, Q.; Gordienko, A.; Wan, X.; Savrasov, S. Y. Calculated Momentum Dependence of Zhang-Rice States in Transition Metal Oxides. *Phys Rev Lett* **2008**, *100* (6), 066406. <https://doi.org/10.1103/PhysRevLett.100.066406>.
- (127) Miura, O.; Fujiwara, T. Electronic Structure and Effects of Dynamical Electron Correlation in Ferromagnetic Bcc Fe, Fcc Ni, and Antiferromagnetic NiO. *Phys Rev B* **2008**, *77* (19), 195124. <https://doi.org/10.1103/PhysRevB.77.195124>.
- (128) Nekrasov, I. A.; Pavlov, N. S.; Sadovskii, M. V. Consistent LDA' + DMFT Approach to the Electronic Structure of Transition Metal Oxides: Charge Transfer Insulators and Correlated Metals. *J. Exp. Theor. Phys.* **2013**, *116* (4), 620–634. <https://doi.org/10.1134/S1063776113030126>.
- (129) Panda, S. K.; Pal, B.; Mandal, S.; Gorgoi, M.; Das, S.; Sarkar, I.; Drube, W.; Sun, W.; Di Marco, I.; Lindblad, A.; Thunström, P.; Delin, A.; Karis, O.; Kvashnin, Y. O.; van Schilfgaarde, M.; Eriksson, O.; Sarma, D. D. High Photon Energy Spectroscopy of NiO: Experiment and Theory. *Phys Rev B* **2016**, *93* (23), 235138. <https://doi.org/10.1103/PhysRevB.93.235138>.
- (130) Lechermann, F.; Körner, W.; Urban, D. F.; Elsässer, C. Interplay of Charge-Transfer and Mott-Hubbard Physics Approached by an Efficient Combination of Self-Interaction Correction and Dynamical Mean-Field Theory. *Phys Rev B* **2019**, *100* (11), 115125. <https://doi.org/10.1103/PhysRevB.100.115125>.
- (131) Mott, N. F. The Basis of the Electron Theory of Metals, with Special Reference to the Transition Metals. *Proc. Phys. Soc. Sect. A* **1949**, *62* (7), 416–422. <https://doi.org/10.1088/0370-1298/62/7/303>.
- (132) Sawatzky, G. A.; Allen, J. W. Magnitude and Origin of the Band Gap in NiO. *Phys Rev Lett* **1984**, *53* (24), 2339–2342. <https://doi.org/10.1103/PhysRevLett.53.2339>.
- (133) Leung, T. C.; Chan, C. T.; Harmon, B. N. Ground-State Properties of Fe, Co, Ni, and Their Monoxides: Results of the Generalized Gradient Approximation. *Phys Rev B* **1991**, *44* (7), 2923–2927. <https://doi.org/10.1103/PhysRevB.44.2923>.
- (134) Perdew, J. P.; Burke, K.; Ernzerhof, M. Generalized Gradient Approximation Made Simple. *Phys Rev Lett* **1996**, *77* (18), 3865–3868. <https://doi.org/10.1103/PhysRevLett.77.3865>.
- (135) Deskins, N. A.; Rousseau, R.; Dupuis, M. Distribution of Ti³⁺ Surface Sites in Reduced TiO₂. *J. Phys. Chem. C* **2011**, *115* (15), 7562–7572. <https://doi.org/10.1021/jp2001139>.
- (136) Shibuya, T.; Yasuoka, K.; Mirbt, S.; Sanyal, B. A Systematic Study of Polarons Due to Oxygen Vacancy Formation at the Rutile TiO₂(110) Surface by GGA +U and HSE06 Methods. *J. Phys. Condens. Matter* **2012**, *24* (43), 435504. <https://doi.org/10.1088/0953-8984/24/43/435504>.
- (137) Wallace, S. K.; McKenna, K. P. Facet-Dependent Electron Trapping in TiO₂ Nanocrystals. *J. Phys. Chem. C* **2015**, *119* (4), 1913–1920. <https://doi.org/10.1021/jp511529u>.
- (138) Chai, Z.; Teobaldi, G.; Si, R.; Liu, L.-M. Subspace Occupancy-Constraining Potentials for Modeling Polaron Formation. *J. Phys. Chem. C* **2021**, *125* (48), 26354–26362. <https://doi.org/10.1021/acs.jpcc.1c07709>.

- (139) Setvin, M.; Franchini, C.; Hao, X.; Schmid, M.; Janotti, A.; Kaltak, M.; Van de Walle, C. G.; Kresse, G.; Diebold, U. Direct View at Excess Electrons in TiO₂ Rutile and Anatase. *Phys Rev Lett* **2014**, *113* (8), 086402. <https://doi.org/10.1103/PhysRevLett.113.086402>.
- (140) Krüger, P.; Bourgeois, S.; Domenichini, B.; Magnan, H.; Chandesaris, D.; Le Fèvre, P.; Flank, A. M.; Jupille, J.; Floreano, L.; Cossaro, A.; Verdini, A.; Morgante, A. Defect States at the TiO₂(110) Surface Probed by Resonant Photoelectron Diffraction. *Phys Rev Lett* **2008**, *100* (5), 055501. <https://doi.org/10.1103/PhysRevLett.100.055501>.
- (141) Pascual, J.; Camassel, J.; Mathieu, H. Fine Structure in the Intrinsic Absorption Edge of TiO₂. *Phys Rev B* **1978**, *18* (10), 5606–5614. <https://doi.org/10.1103/PhysRevB.18.5606>.
- (142) Amtout, A.; Leonelli, R. Optical Properties of Rutile near Its Fundamental Band Gap. *Phys Rev B* **1995**, *51* (11), 6842–6851. <https://doi.org/10.1103/PhysRevB.51.6842>.
- (143) Park, S.-G.; Magyari-Köpe, B.; Nishi, Y. Electronic Correlation Effects in Reduced Rutile TiO₂ within the LDA+*U* Method. *Phys Rev B* **2010**, *82* (11), 115109. <https://doi.org/10.1103/PhysRevB.82.115109>.
- (144) Beattie, J. K.; Best, S. P.; Skelton, B. W.; White, A. H. Structural Studies on the Caesium Alums, CsM[SO₄]₂·12H₂O. *J. Chem. Soc. Dalton Trans.* **1981**, No. 10, 2105–2111. <https://doi.org/10.1039/DT9810002105>.
- (145) Aakesson, R.; Pettersson, L. G. M.; Sandstroem, M.; Wahlgren, U. Theoretical Calculations of the Jahn-Teller Effect in the Hexahydrated Copper(II), Chromium(II), and Manganese(III) Ions, Hexaaquacopper(2+), Hexaaquachromium(2+) and Hexaaquamanganese(3+), and Comparisons with the Hexahydrated Copper(I), Chromium(III), and Manganese(II) Clusters. *J. Phys. Chem.* **1992**, *96* (1), 150–156. <https://doi.org/10.1021/j100180a031>.
- (146) Li, J.; Fisher, C. L.; Chen, J. L.; Bashford, D.; Noodleman, L. Calculation of Redox Potentials and pKa Values of Hydrated Transition Metal Cations by a Combined Density Functional and Continuum Dielectric Theory. *Inorg. Chem.* **1996**, *35* (16), 4694–4702. <https://doi.org/10.1021/ic951428f>.
- (147) Kallies, B.; Meier, R. Electronic Structure of 3d [M(H₂O)₆]³⁺ Ions from ScIII to FeIII: A Quantum Mechanical Study Based on DFT Computations and Natural Bond Orbital Analyses. *Inorg. Chem.* **2001**, *40* (13), 3101–3112. <https://doi.org/10.1021/ic001258t>.
- (148) Yang, Y.; Ratner, M. A.; Schatz, G. C. Multireference Ab Initio Study of Ligand Field d–d Transitions in Octahedral Transition-Metal Oxide Clusters. *J. Phys. Chem. C* **2014**, *118* (50), 29196–29208. <https://doi.org/10.1021/jp5052672>.
- (149) Lever, A. B. P. *Inorganic Electronic Spectroscopy*, 3. impr.; Studies in physical and theoretical chemistry; Elsevier: Amsterdam, 1984.
- (150) Aakesson, R.; Pettersson, L. G. M.; Sandstroem, M.; Wahlgren, U. Ligand Field Effects in the Hydrated Divalent and Trivalent Metal Ions of the First and Second Transition Periods. *J. Am. Chem. Soc.* **1994**, *116* (19), 8691–8704. <https://doi.org/10.1021/ja00098a032>.